The Application of a Five-Hole Probe Wake-Survey Technique to the Study of Swept Wing Icing Aerodynamics

Christopher W. Lum* and Navdeep Sandhu†
University of Washington, Seattle, WA, 98195, USA

Jeffrey M. Diebold‡ and Brian S. Woodard§
University of Illinois at Urbana-Champaign, Urbana, Illinois, 61801, USA

and Michael B. Bragg¶
University of Washington, Seattle, WA, 98195, USA

This paper describes a wake survey system used to improve the understanding of the underlying flowfield and aerodynamics of a swept wing with ice accretions. This system allows the rapid collection and analysis of large amounts of flowfield data by utilizing an array of five-hole probes on a precisely controlled traverse arm. Flowfield structure on the surface of the wing is acquired using an oil flow visualization technique and correlated to the associated wake survey. This method allows quantitative calculations such as spanwise lift and drag to be compared with qualitative measurements and observations to enhance the understanding of the aerodynamics of wings containing ice accretions. Wind tunnel tests for a range of configurations are presented and analyzed in this paper. Results based on this wake survey method are compared with traditional measurement techniques such as force balance measurements to assess their accuracy.

Nomenclature

AR	Aspect ratio
C_{di}	Sectional induced drag coefficient
C_{dp}	Sectional profile drag coefficient
c_l	Sectional lift coefficient
C_{pt}	Coefficient of total pressure
C_{ps}	Coefficient of static pressure
D_i	Induced drag (N)
D_p	Profile drag (N)
F_T	Traverse coordinate frame
L	Lift (N)
M	Freestream Mach number

*Research Assistant Professor, William E. Boeing Department of Aeronautics and Astronautics, University of Washington; Guggenheim Hall Room 211, Box 352400, Seattle, WA 98195-2400, AIAA member.

†Research Assistant, William E. Boeing Department of Aeronautics and Astronautics, University of Washington; Guggenheim Hall Room 211, Box 352400, Seattle, WA 98195-2400, AIAA member.

‡Research Assistant, Department of Aerospace Engineering, 306 Talbot Lab, 104 S. Wright St., AIAA member.

§Research Associate, Department of Aerospace Engineering, 306 Talbot Lab, 104 S. Wright St., AIAA member.

¶Dean, College of Engineering and Professor, William E. Boeing Department of Aeronautics and Astronautics, University of Washington; Loew Hall Room 371, Box 352180, Seattle, WA 98195-2180, AIAA fellow.

$P_{t\infty}$	Freestream total pressure (Pa)
P_t	Total pressure
Re	Reynolds number based on mean aerodynamic chord
ROI	Wake region of interest
S_2	Cross-sectional area of wake survey measurement plane (m^2)
u_b	Wake blockage velocity (m/s)
u^*	Artificial velocity (m/s)
U_∞	Freestream velocity (m/s)
y	Distance from wing root to local spanwise location (m)
x_{ws}	Streamwise direction in wake survey coordinate frame
y_{ws}	Spanwise direction in wake survey coordinate frame
z_{ws}	Wing-normal direction in wake survey coordinate frame
x_{TS}	Streamwise direction in test section coordinate frame
y_{TS}	Spanwise direction in test section coordinate frame
z_{TS}	Wing-normal direction in test section coordinate frame
α	Corrected angle of attack (degrees)
λ	Taper ratio
Λ_{LE}	Leading-edge sweep angle
ψ	Stream function (m^2/s)
ρ	Density (kg/m^3)
ζ	Vorticity (m^2/s)

I. Introduction

Airframe icing continues to present a challenge to aircraft designers, manufacturers, and regulatory agencies. The accretion of ice, especially on lifting surfaces, can have serious consequences for an aircraft, as even small ice accretions can lead to a significant decrease in maximum lift, increase in drag and loss of control authority on some configurations. This work aims to better understand the aerodynamic flowfields of iced swept wings by probing the wake of these configurations. Measuring quantities such as pressure, velocity, and angularity of the wake allow researchers to see larger flowfield structures and correlate these to corroborating measurements such as lift and drag from the balance. In addition to computing total lift and drag, the wake survey method allows the the lift and drag to be decomposed into spanwise distributions. This allows greater correlation between flowfield features observed on the wing and their resulting contributions to aerodynamic forces.

A. Problem Statement

This paper presents methodology for understanding the structure of the flowfield generated by an iced, swept wing. The primary tool for assessing the structure of the flowfield is an array of three individual five-hole probes attached to the end of a positionable traverse/swing arm system. This system is used to provide high resolution and accurate measurements of flowfield quantities such as total pressure, flow angularity, etc. at precise locations in the wake. Oil flow visualization is a supplemental tool used to understand flowfield structure on the wing surface and is presented in conjunction with the associated wake survey data.

This work is part of a larger research effort to understand aerodynamic effects of ice accretions on swept wings. This includes Reynolds and Mach number effects, the underlying flowfield physics, and differences from the airfoil/infinite-wing case. The flowfield of a swept wing is considerably more complicated as it involves fully 3D flow and interactions. As such, ice shapes observed on swept wings have considerable and complex geometry. This complexity makes modeling and recreating these geometries on new configurations and conditions challenging. One of the major goals of the project is to understand the requisite fidelity of these ice accretions necessary to reproduce similar aerodynamic effects. If it can be shown that lower fidelity versions of these ice shapes behave similarly from an aerodynamic perspective, stakeholders interested in aircraft icing can use simplified geometries for their analyses. This paper proposes a tool to help enable flowfield comparisons between high-fidelity and low-fidelity versions of these ice shapes.

On a related note, another goal of the larger project is to improve the fidelity of experimental and

computational simulation methods for swept-wing ice accretion formation and the resulting aerodynamic effect. The work described in this paper focuses on developing experimental methods to survey the wake of a swept wing with ice accretions to help understand the underlying flowfield structure and its influence on the 3D aerodynamic performance of the wing. The ability to develop spanwise lift and drag distributions will provide insight into the effects of the ice accretions. This will then be correlated with force balance data to validate the process and its accuracy.

B. Literature Review

Previous work by Khodadoust et al.[1] and Bragg et al.[2,3] discussed the underlying flowfield features that are responsible for the measured performance degradation on 2D airfoils. Diebold et al.[4] proposed an ice accretion classification system based on the aerodynamic effects of the ice. The aerodynamics of a swept wing with ice accretions at low Reynolds number were also investigated by this group.[5]

This work was recently extended in a collaboration involving the Federal Aviation Administration (FAA), the University of Washington (UW), the University of Illinois at UrbanaChampaign (UIUC), the University of Virginia (UVA), NASA, and the Office National d'Etudes et de Recherches Aerospatiales (ONERA) to investigate various aspects of icing aerodynamics. This work involved developing representative ice accretions on full scale, swept-wing models[6,7] at NASA's Icing Research Tunnel (IRT).[8] These geometries were processed and developed into full span ice shapes.[9] Simulations of the conditions used to generate these shapes were performed[10] and combined with various techniques[11,12] to predict these shapes.[13,14] Tests at lower *Re* were conducted[15,16] to evaluate the performance of swept wings with these various ice shapes attached.

The results presented in this paper are primarily based on work by Diebold[17] that utilized similar techniques to perform wake surveys of iced swept wings using a single probe.[18,19]

In 2001, Lynch and Khodadoust[20] reviewed the effects of ice on the performance of lifting surfaces.

Work by Papadakis[21] et al.[22] measured the performance effects of various ice accretions on a swept wing with $\Lambda_{LE} = 28^o$, AR = 6.8, $\lambda = 0.4$, and a modern transonic airfoil.

II. Model Description

A. Wing Model

As mentioned previously, this paper is part of a larger research project focused on swept-wing icing. This larger research project chose to use a 65% scale version of the Common Research Model (CRM)[23] as the baseline configuration. This 65% version is referred to as the CRM65. The 1-g wing loading in the CRM was removed so that there is no dihedral and the leading edge is nearly a straight line. The wing retains the twist and taper of the CRM. An 8.9% version this CRM65 configuration was developed for use in the Walter H. Beech Memorial Wind Tunnel at Wichita State University (WSU) and is hereafter referred to as the WSU model. The leading edge of the model is removable and allows different ice shapes to be attached and tested on the model. The model has a splitter plate to mitigate boundary layer effects.[24] Both a CAD model and the model installed in the WSU wind tunnel test section are shown in Fig. 1. Further details of the model can be found in a report by Woodard et al.[25]

B. Ice Shapes

Removable leading edges representing different ice shapes are generated and tested on the WSU model. These ice shapes were experimentally obtained at NASA's IRT, laser-scanned to digitize the geometry, and processed into CAD files that were mated to the WSU model leading edge. Other ice shapes were generated using CFD techniques to serve as comparison cases. Two fidelities of ice shape were tested, with the goal of comparing the flowfields and concluding if low-fidelity ice shapes can aerodynamically represent high-fidelity ice shapes of the same variety. A high-fidelity shape is a 3D recreation of an ice accretion that has been laser-scanned from real ice. A low-fidelity (low-fi) shape is one that does not maintain all the 3D features and roughness of the original ice accretion, but maintains the same general shape and some large scale features. The grit on an ice shape refers to 3D texture added to low-fi ice shapes for testing to help simulate the roughness of the high-fidelity shapes. The physical construction of the low-fi shapes is faster and cheaper than creating a high-fidelity ice shape; thus, low-fi shapes are preferred for testing, assuming that they can recreate the flowfield of their high-fidelity counterparts. Examples of both fidelities of the maximum scallop

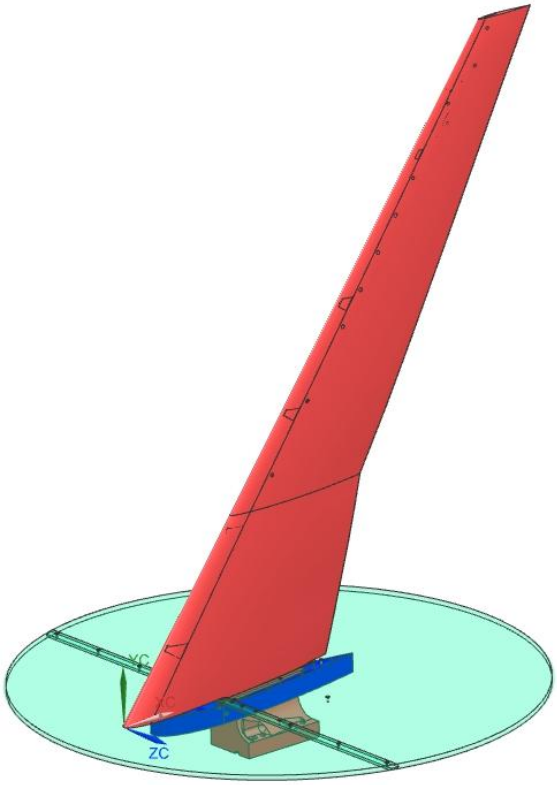

(a) CAD rendering of the WSU model.

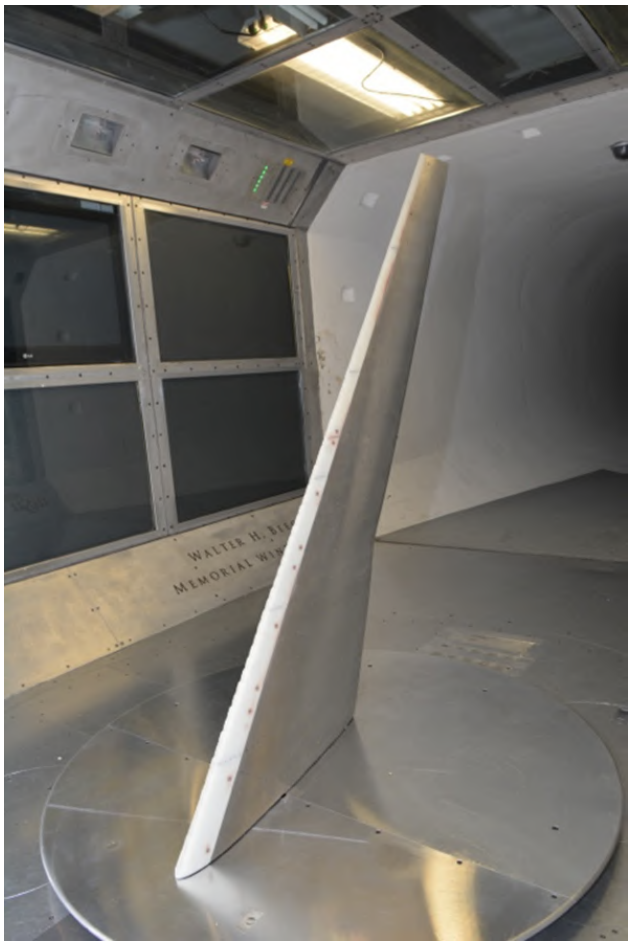

(b) WSU model installed in the Walter H. Beech Memorial Wind Tunnel.

Figure 1. The WSU model is an 8.9% version of the CRM65 model designed for testing in the WSU tunnel.

shape are shown in Fig. 2. The specifics of the geometry and generation of these shapes are detailed by Camello et al.[9] An example set of printed ice shapes is shown in Fig. 3. The ice shapes are 3D printed using a stereolithography technique (SLA) using the Somos NeXt material. These shapes are instrumented with pressure taps and attached to the model for testing.

III. Secondary Experimental Methods

Some supplemental experimental techniques and systems are described in this section. These are presented before the primary experimental method (the wake survey system) as it provides relevant background material.

A. Wind Tunnel

Tests were conducting at the Wichita State University (WSU) Walter H. Beech Memorial Wind Tunnel[26] hereafter referred to as the WSU tunnel. This facility provides private industry, government agencies, and educational institutions with aerodynamic testing capabilities. The WSU Tunnel is a subsonic, closed-return aerodynamic research, development, and production wind tunnel with a test section size of $7 \times 10 \times 12$ feet. The tunnel can control steady wind speeds from 20 to 230 mph (Re from 0.2×10^6 to 1.8×10^6 and M from 0.09 to 0.26). It has a variety of internal and external balances for customer use. The primary balance is a six-component, pyramidal under-floor external balance that can capture highly accurate force and moment

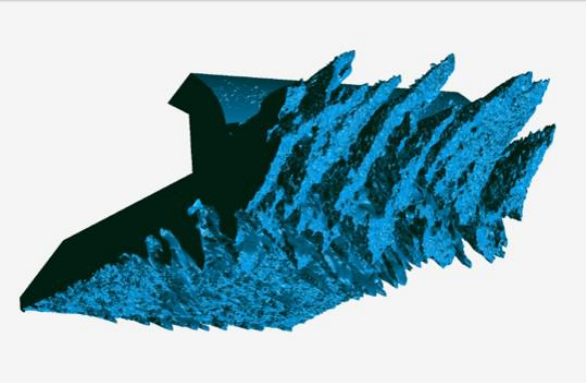

(a) Computerized example of a high-fidelity ice shape.

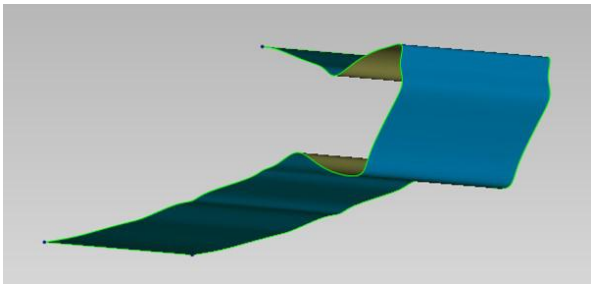

(b) Computerized example of a low-fidelity ice shape.

Figure 2. A high-fidelity and low-fidelity version of the maximum scallop ice shape. The low-fidelity shape does not retain the 3D features of the high-fidelity shape.

Figure 3. A fully instrumented ice shape of the maximum scallop configuration. Notice that the complete ice shape is broken into an inboard and outboard shape.

data for the model. Other integrated measurement tools provide for simultaneous measurement of hundreds of pressures and other sensors. Also available is an automated traverse system, which is used extensively in this research. Raw balance measurements at the WSU tunnel can be corrected for various effects such as balance interactions and boundary effects.[27] Note that in these analyses, uncorrected data was used for comparison as it is more appropriate. These analyses and associated discussion are presented in Section V. Details regarding the setup of the test have been documented in previous publications.[25]

B. Surface Oil Flow Visualization

Surface oil flow visualization was used to gain a qualitative understanding of the flowfield at the wing's surface. The technique used in this study follows the procedure documented by Winkler.[28] The procedure for application of the oil flow was described by Diebold[18] and was followed in this test with the small improvement of using a paint roller to apply the mixture as opposed to an airbrush. Results of this are shown in Section VI.

C. Laser Scanning and Tracking System

This work made use of several laser scanning and tracking systems to obtain precise measurements of various geometry associated with the test. As part of test preparation, a Leica T-Scan 5[29] hand-held scanner was used to scan the geometry of the probe array in order to obtain the relative location of the probe tips with respect to the traverse arm (Fig. 4). In addition, other geometry associated with the probe array was scanned using a various Leica scanners to place the traverse system in the tunnel's coordinate system (Fig. 5(a)).

Because the probe array is somewhat large, mounted at a non-negligible distance from the pivot point, and is subject to moderate dynamic pressures, the traverse arm may bend or deflect during wind-on runs. To combat this problem, the position of the wake array was measured using a Leica AT901[30] laser tracking system with respect to the test section (Fig. 7(a)). This allows the deflection to be measured and corrected.

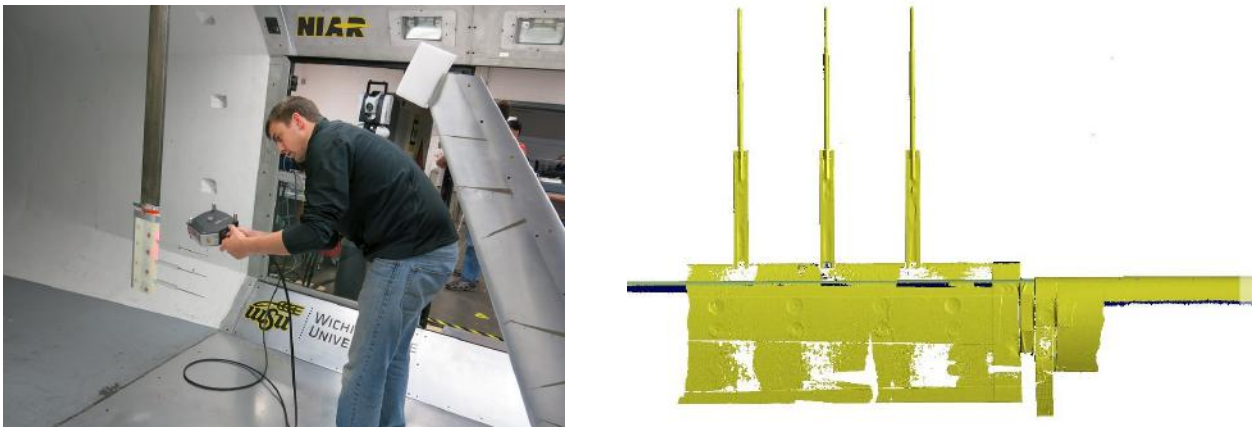

(a) Using a Leica T-Scan 5 to scan the probe array.

(b) Resulting point cloud representation of the probe array.

Figure 4. Obtaining precise measurements of the location of the probe tips with respect to the traverse arm.

IV. Wake Survey System: Physical Description

The main experimental apparatus used in this work was an array of three probes attached to the WSU traverse system. Each probe in the array is a five-hole probe that can measure flow velocity, pressure, and angularity. This probe array can be positioned to precise locations in the test section in order to acquire data in the wake in an automated fashion. The wake survey system is comprised of various components.

A. Traverse System

The WSU tunnel has a traverse arm used for introducing probes into the test section (Fig. 5(a)). This traverse arm is also referred to as the swing arm. Note that the traverse system moves in a polar fashion rather than in a rectangular grid. In other words, the arm can be rotated about a pivot point near the ceiling of the tunnel and the radius of the arm can be changed as shown in Fig. 6.

The angular range of the traverse arm is approximately +/- 40 deg. Note that the arm can be pinned in either an upper (arm is less extended) or lower (arm is more extended) position. In either case, the radial extension of the arm can be controlled to allow approximately 47 inches of travel with significant overlap as shown in Fig. 6(a) and Fig. 6(b). This arm is mounted to a fixed lateral position in the test section but has the ability to move upstream/downstream.

B. Wake Array

The tip of the traverse arm holds three five-hole probes as shown in Fig. 5(b). This is referred to as the probe array. The probes used for this study are Aeroprobe straight five-hole probes. These are calibrated by Aeroprobe[31] for the appropriate Mach number at a variety of flow angles. This calibration is used to generate a sector interpolant method[32] for mapping pressures of individual holes on each probe to relevant physical properties such as flow angle and pressure. The probe holder is covered with a 3D-printed (SLA)

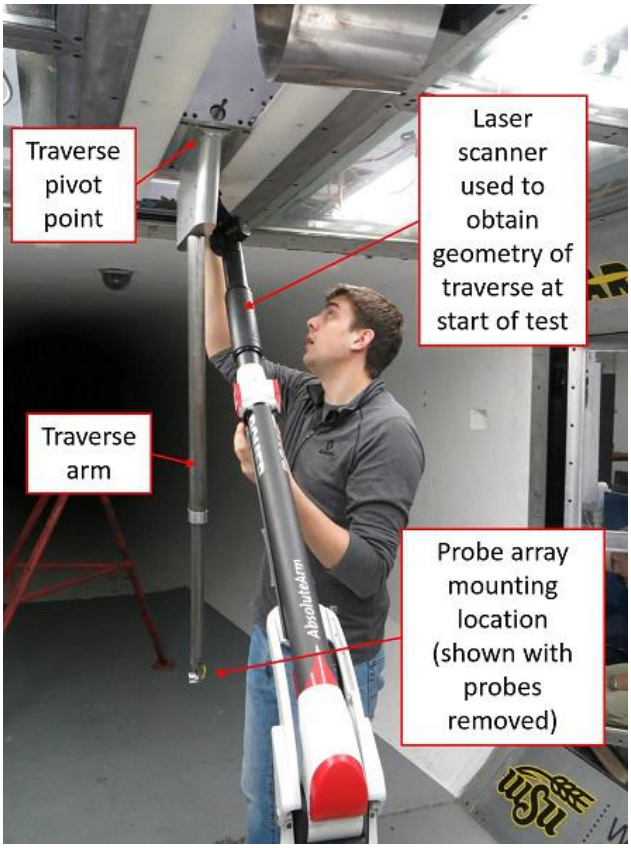

(a) View from the bellmouth looking towards the diffuser of the test section. The traverse arm extends from the ceiling and is located downwind of the model.

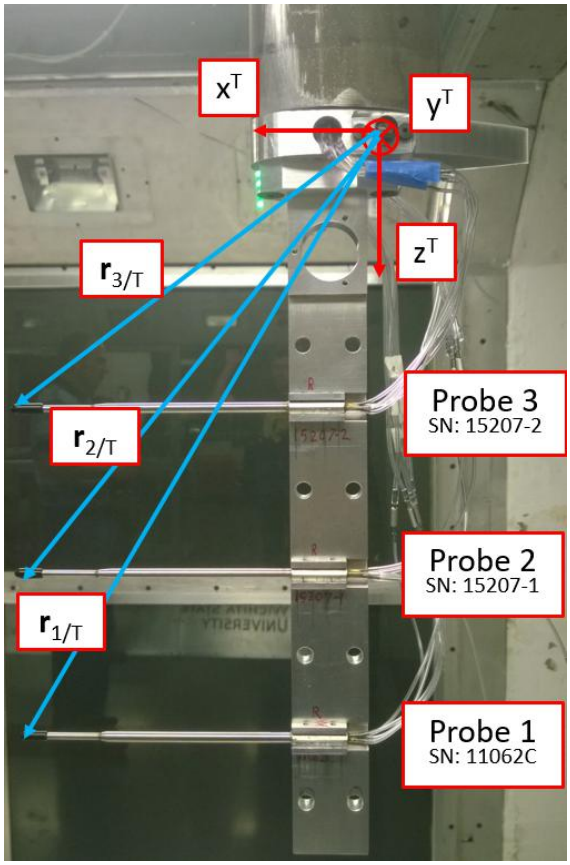

(b) 3-probe system without aerodynamic fairing. Note the location of the laser tracker at the origin of F_T (the coordinate frame attached to the traverse arm).

Figure 5. Setup of traverse arm with the probe array installed.

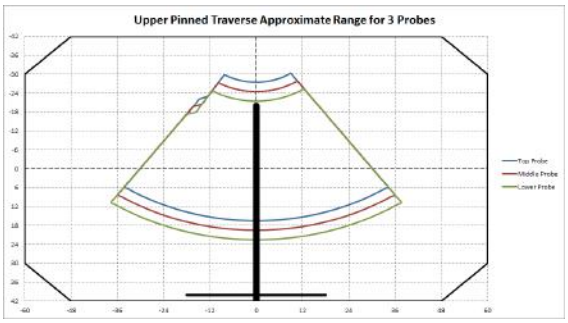

(a) Coverage of the probe system when arm is pinned in the upper configuration

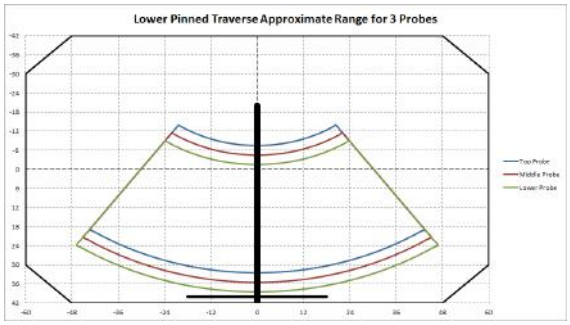

(b) Coverage of the probe system when arm is pinned in the lower configuration

Figure 6. Coverage of the wake survey system. The wing and splitter plate are drawn the the vertical and horizontal black lines, respectively.

fairing (Fig. 7(b)). The entire probe holder and fairing system was designed by the UW and UIUC and is engineered to minimize the amount of upstream flow disturbances at the tip of the probes. The complete wake survey system installed in the tunnel behind the model is shown in Fig. 7(b).

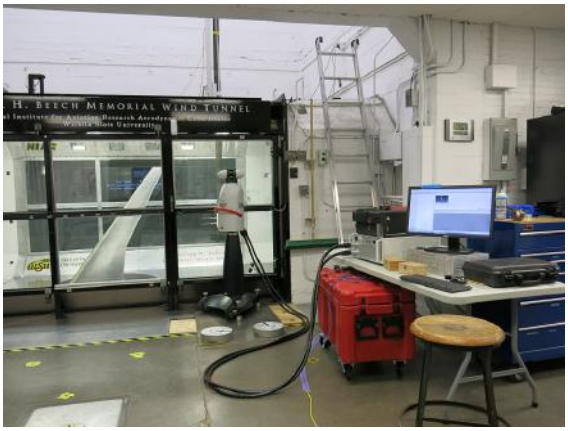

(a) Overall position tracking system installed in the tunnel. Note the AT901 near the window and attached to the associated data acquisition computers.

(b) Wake survey system installed in tunnel behind model.

Figure 7. The wake survey system installed in the tunnel.

V. Wake Survey System: Data Reduction

A. Data Acquisition

Various data sets were collected. These include wake survey pressure measurements, force balance data, various flow visualization, and other measurements. The various data acquisition techniques are detailed in this section.

1. Pressure Measurements

Pressures from each probe are recorded on a Scanivalve DSA-3217 with 1 psid range. These are acquired and averaged for each data point. Various corrections were applied to correct these measurements to equivalent free stream conditions.

2. Probe Path Planning

The goal of the wake survey system is to obtain data in desired locations in the wake. To this end, a path planning system was developed where the user is able to specify one or more wake regions of interest (ROIs). These rectangular areas denote regions where wake measurements should be made and are aligned with the spanwise (y_{TS}) and transverse (z_{TS}) plane of the wake. In addition to the ROIs, the user specifies a desired spacing in both directions which denotes the desired spatial resolution of data in the wake plane. Ideally, the system would gather data within the ROIs at these spacings on a perfectly rectangular grid. However, given the polar setup of the system and the fact that the spacing between the probes is fixed, a perfectly rectangular grid is infeasible. Instead, the path planner will position the wake survey system in an approximately rectangular grid as shown in Fig. 8(a). This system calculates the desired position of the traverse system such that probe 1 is positioned in a perfectly rectangular grid as desired. Note that as a consequence, probe 2 and 3 follow a slightly curvilinear path with spacing slightly tighter than desired. An example of a coarse survey is shown in Fig. 8(b). In this example, the user specifies two ROIs. The ROI corresponding to the tip vortex of the wing has a much finer spatial resolution than the inboard ROI. Notice that probe 1 (red) is placed in a perfectly rectangular pattern but probe 3 moves in a somewhat curvilinear path (blue).

B. Lift and Drag From Wake Measurements

Reducing wake survey data to lift and drag data is done by performing a control volume analysis around the wing, applying conservation of momentum, and making several assumptions. This process was developed by Betz[33] and later by Maskell,[34] and was summarized by Diebold.[18] A summary of the resulting wake integrals

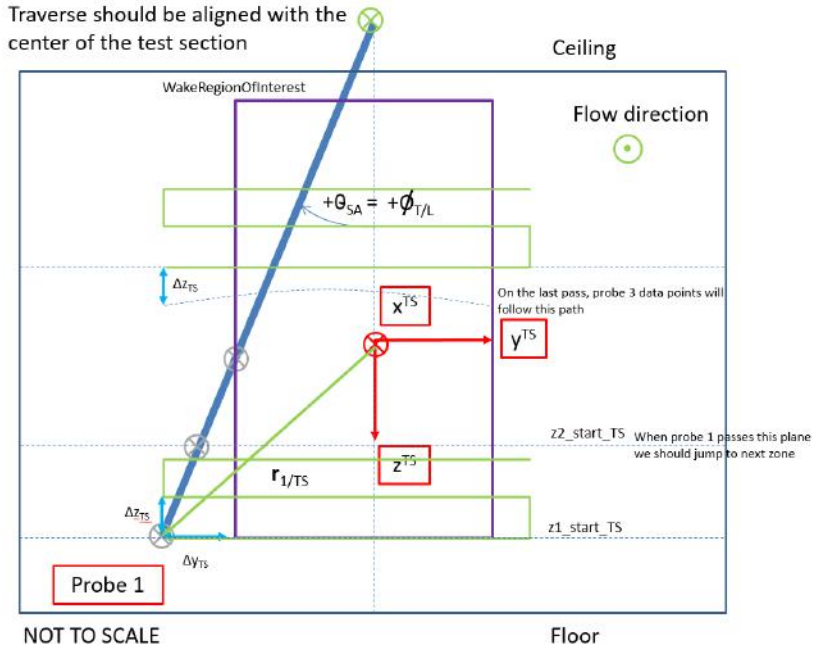

(a) The path planning algorithm to position the probes in the wake region of interest.

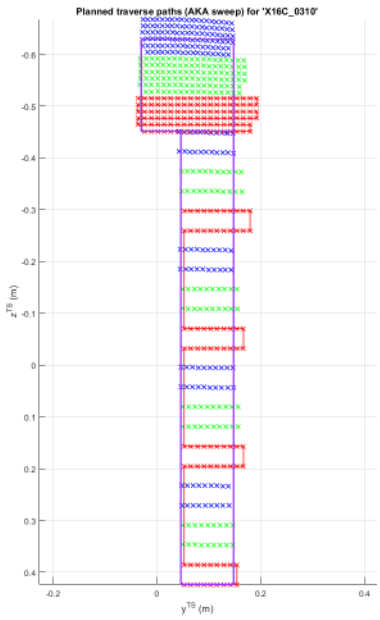

(b) A coarse survey over two ROIs. Red = probe 1, green = probe 2, blue = probe 3.

Figure 8. Path planning algorithm and desired trajectory for a probe survey.

for induced drag, profile drag, and lift are provided here. The coordinate system used for the derivation of the wake survey integrals is different than that defined for the testing; the coordinates are given in Fig. 9. The domain of integration for each wake integral is the wake behind the wing.

$$D_i = \frac{\rho}{2} \iint_W \psi\zeta \, dy_{ws} \, dz_{ws} \tag{1}$$

$$D_p = \iint_W ((P_{t\infty} - P_t) + \frac{\rho}{2}(u - u^*)(u + u^* - 2(U_\infty + u_b))) \, dy_{ws} \, dz_{ws} \tag{2}$$

$$L = \rho U_\infty \iint_W y\zeta \, dy_{ws} \, dz_{ws} \tag{3}$$

Several variables are introduced in these equations. ψ is the stream function of the transverse flow and is found as:

$$\nabla^2 \psi = -\zeta \tag{4}$$

This is solved using a numerical iteration method. ζ is the vorticity in the streamwise direction, given as:

$$\zeta = \frac{\partial w}{\partial y} - \frac{\partial v}{\partial z} \tag{5}$$

Where v and w define the flow velocities in the spanwise direction and perpendicular to the test section side wall (the y_{ws} and z_{ws} directions), respectively.

To reduce the amount of data that needs to be taken by the wake survey, an artificial velocity u^* is defined such that it is equal to the freestream velocity outside of the wake, causing the integrand of the profile drag equation to go to zero in non-wake regions (as the freestream total pressure and measured total pressure should be equal outside of the wake as well). This artificial velocity is given by:

$$u^* = u^2 + \frac{2}{\rho}(P_{t\infty} - P_t) \tag{6}$$

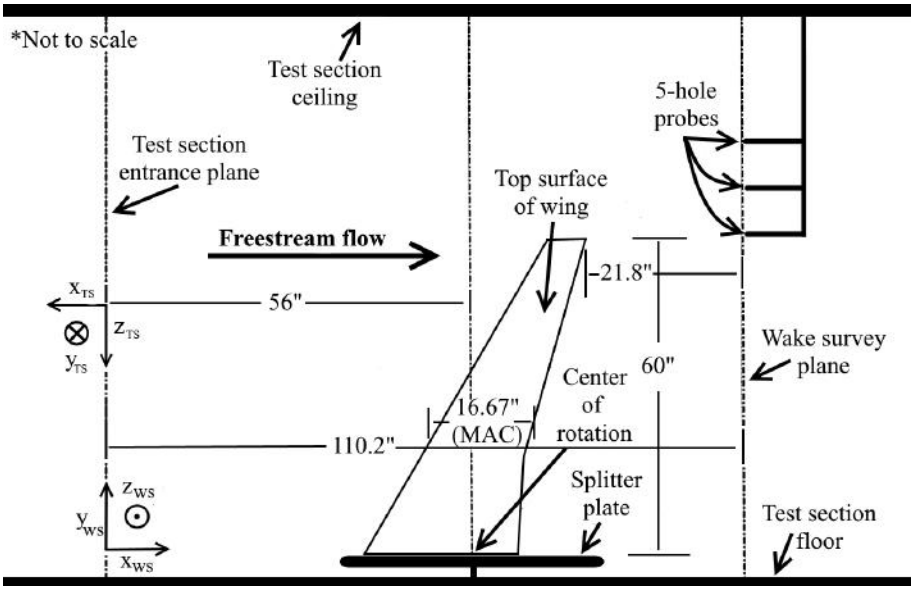

Figure 9. Coordinate system used to carry out the integrals to find lift, induced drag, and profile drag; this system is denoted with the subscript WS. This coordinate system differs from the system used to take the wake survey measurements, which is shown and denoted by the TS subscript.

Where u is the local streamwise velocity. Finally, the wake blockage velocity u_b is defined as:

$$u_b = \frac{1}{2S_2} \iint_W u^* - u \, dy \, dz \tag{7}$$

With S_2 being the cross-sectional area of the test section at the wake survey measurement plane. The vorticity outside of the wake is ideally zero as well, meaning all the wake integrals can be taken over the entire plane S_2 without accounting for freestream data.

C. Data Analysis Algorithm

As discussed previously, data were not acquired on a perfectly rectangular grid (Figure 8(b)). However, the wake integrals in Eq. 1-Eq. 3 are most easily performed using numerical integration on a rectangular grid. Therefore, the data were interpolated onto a rectangular grid using Matlab's scatteredInterpolant function.

Due to the large spanwise length of the wake, the wake survey physically took place as two individual runs. As shown in Fig. 6, the wake survey rake had an upper and lower position for data collection. Thus, both sets of data (the inboard and outboard run) had to be combined to form the full wake data set. Points that overlapped had their measurements averaged to form the data set that was interpolated onto the rectangular grid. These steps introduced some error into the analysis, but due to the fine grid spacing of the collected data points, this error was assumed small.

Before data could be integrated, the boundary of the wake was identified. In theory, the integrands of the wake integrals should be zero outside of the wake itself. Therefore, integrating over the entire measurement plane (the ROIs in Fig. 8(b)) should yield the same result as integrating over just the wake region. However, due to experimental error, this is not true. Thus, the edge of the wake had to be found so the numerical integration could be performed over just the area of the wake to avoid introducing erroneous forces due to the measurement error outside the wake. Identification of the wake was done by looking at the total pressure coefficient (the ratio of the total pressure in the wake to the freestream dynamic pressure) at each point in the flow. In the wake, there is a pressure loss associated with drag; in the freestream, there would be no pressure loss. Any point in the flow with a total pressure coefficient equal to or greater than one (possible due to slight measurement inaccuracies) are considered the freestream. The wake integrands in these regions were set to zero, ensuring the only components contributing to integration were in the wake of the model. An example of the data before and after this process is shown in Figs. 10 and 11. A small region near y/b = 0.08 and z/b = -0.05 shows a total pressure coefficient slightly lower than one; this data was assumed to be

experimental error and was removed heuristically prior to executing the previously described wake finding algorithm.

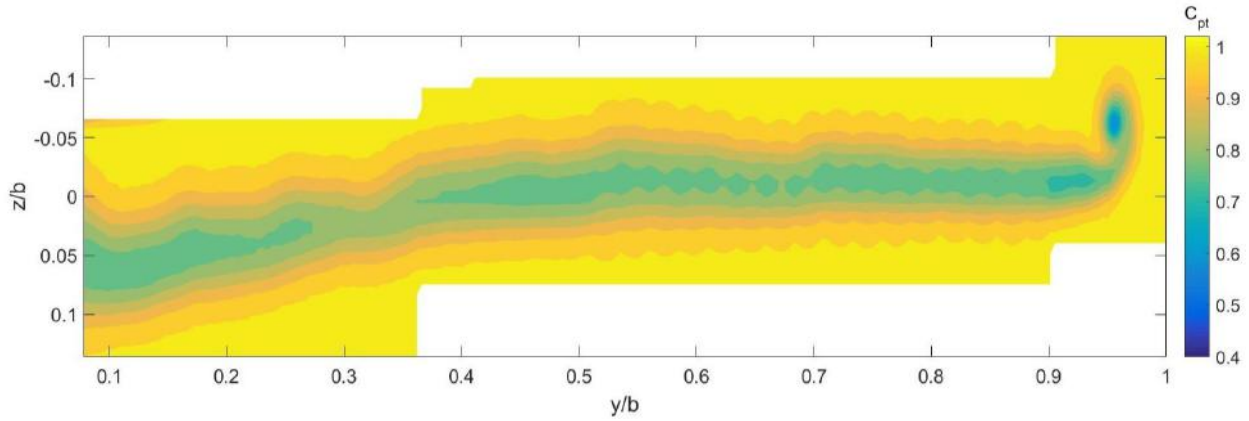

Figure 10. An example of a contour of total pressure coefficient before the edge of the wake is found. The configuration shown is the maximum scallop ice shape at $\alpha = 4.8$ degrees, $Re = 1.6 \times 10^6$, and $M = 0.18$. Notice that data is acquired over the entire ROI.

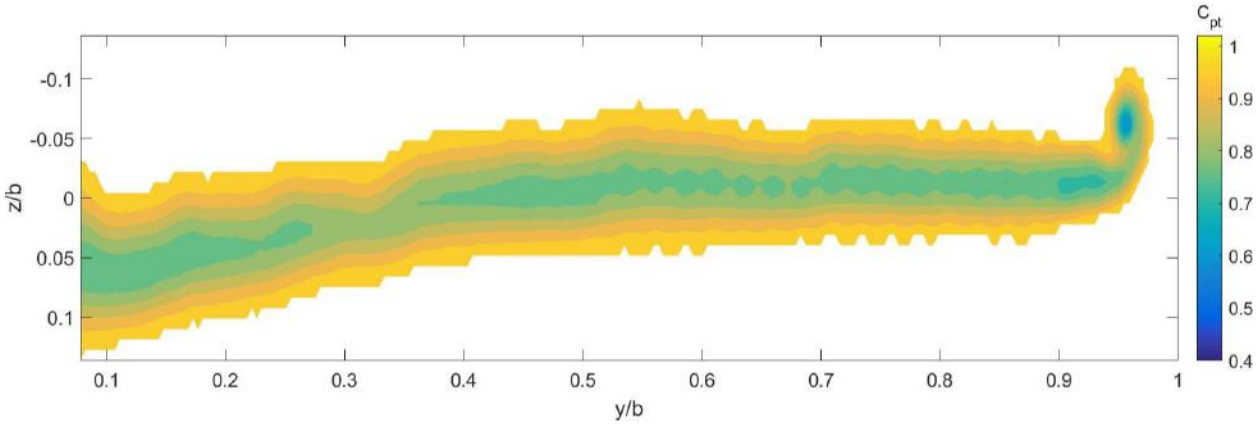

Figure 11. An example of a contour of total pressure coefficient after the edge of the wake is found. The configuration shown is the maximum scallop ice shape at $\alpha = 4.8$ degrees, $Re = 1.6 \times 10^6$, and $M = 0.18$.

Both the vorticity and the stream function had to be calculated before integration could occur. To calculate vorticity, the numerical derivatives of the v and w components of velocity were found using a second-order central differencing method. Then, vorticity was found directly from Eq. 5.

Calculating stream function was more complex; the computational domain had to be extended from the rectangular data region to the tunnel walls to ensure that the proper boundary conditions (Ψ is equal to zero on the tunnel walls) were met. This is possible because the vorticity is zero outside of the wake, and from Eq. 4, this sets the forcing function to zero as well. From here, the successive over-relaxation (SOR) method was used to calculate the stream function iteratively; the SOR method is an offshoot of the Gauss-Seidel iterative method that leads to faster convergence of a numerical solution. The SOR parameter was chosen by trial.

Integration was performed using the numerical trapezoidal method in both dimensions of the wake. This resulted in a single value for lift, induced drag, and profile drag. To find sectional induced drag coefficients and sectional profile drag coefficients, Eqs. 1 and 2 were used, but only a single integration was performed in the direction normal to the wing at each given spanwise location, resulting in a spanwise distribution. Sectional lift coefficient was found via classical wing theory and involved finding the spanwise circulation distribution from the spanwise vortex strength distribution. The vortex strength distribution, γ, was calculated by taking a single numerical integral of the vorticity perpendicular to the surface of the wing (in the z_{ws} direction) at a given spanwise location. The circulation distribution was then found as

$$\Gamma = \int_0^{y_{ws}} \gamma dy_{ws} \tag{8}$$

Using spanwise circulation and chord distribution, the sectional lift coefficient is found

$$c_l = \frac{2\Gamma}{U_\infty c} \tag{9}$$

where c represents the chord at a given spanwise location.

VI. Results

Multiple icing configurations were tested with the wake survey system. All configurations tested are shown in Table 1. This paper presents detailed results for the clean leading edge, high-fidelity maximum scallop (maximum scallop), low-fidelity streamwise with grit (low-fi streamwise with grit), and low-fidelity maximum scallop with grit (low-fi maximum scallop with grit) configurations at $\alpha = 4.8$ degrees, $Re = 1.6 \times 10^6$, and $M = 0.18$. Computerized representations of the high and low-fi maximum scallop ice shapes are shown in Fig. 2, while the low-fi streamwise ice shape is shown in Fig. 12.

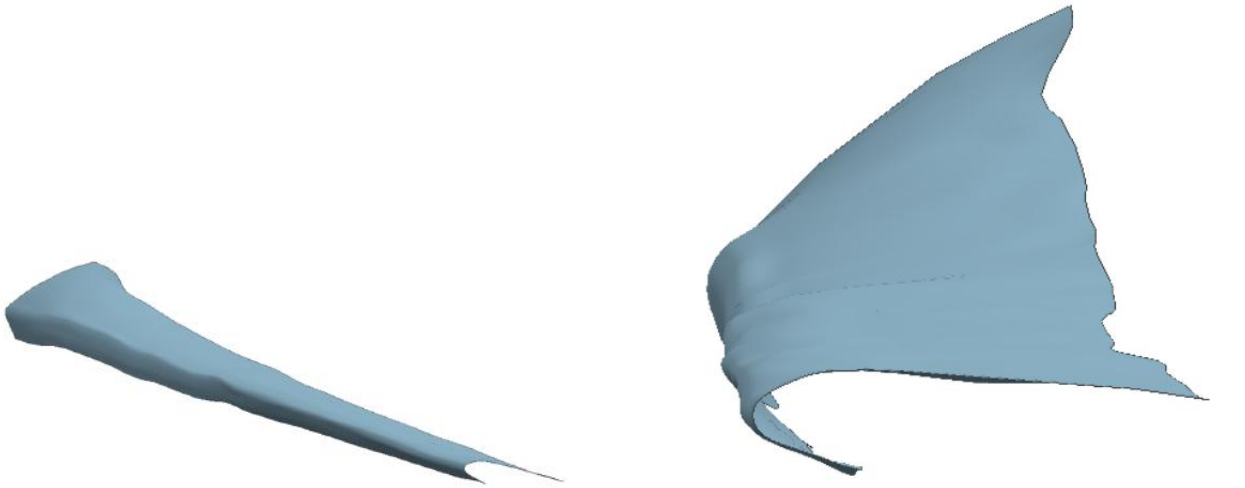

(a) An isometric, full-span view of the low-fi streamwise ice shape.

(b) A view of the low-fi streamwise ice shape from the wing tip, looking inboard.

Figure 12. A computerized representation of the low-fi streamwise ice shape is shown in two orientations.

Table 1. This table lists all of the ice shapes tested with the wake survey system and the angle of attack of the wing for each test. All tests were conducted at $Re = 1.6 \times 10^6$, and $M = 0.18$.

Ice Shape	α **(degrees)**
Clean Leading Edge	0.6, 2.7, 4.8, 6.9, 8.9, 10.9
Maximum Scallop (high-fidelity)	0.6, 2.7, 4.8, 6.9, 7.9
2D Smooth Maximum Scallop with grit (low-fi)	2.7, 4.8, 6.9, 7.9
2D Smooth Maximum Scallop (low-fi)	4.8, 6.9
Streamwise Shape	6.9, 8.9
2D Streamwise Shape with grit (low-fi)	4.8, 6.9, 8.9

A. Wake Survey Calculations Compared to Force Balance Measurements

The plots shown in Figs. 13 to 16 compare the total lift and drag coefficients at various angles of attack from the force balance and the wake survey for the clean leading edge, maximum scallop, low-fi streamwise with grit, and low-fi maximum scallop with grit configurations. Overall, there is an agreement between the wake survey and the force balance for the total lift and drag of the wing. The wake survey, across a variety of icing configurations, agreed well with force balance data for several angles of attack. Figure 14(b) shows that the lift calculations for the maximum scallop configuration agreed well with force balance data for low angles of attack; the wake survey calculations noticeably diverged from the force balance at $\alpha = 4.8$ degrees. The lift and drag calculated by the wake survey for all configurations tended to be higher than the force balance measurements.

Table 2 lists error in the total lift and total drag between the wake survey calculations and force balance measurements for the clean leading edge, maximum scallop, low-fi streamwise with grit, and low-fi maximum scallop with grit configurations. Root mean square (RMS) errors are given for all angles of attack tested with the wake survey system for each configuration. The data in Table 2 presents results for $\alpha = 4.8$ degrees, $Re = 1.6 \times 10^6$, and $M = 0.18$, as this is the most common angle of attack across all configurations. Wake survey calculations agree to within about 16% for drag and within 7.2% for lift for the configurations presented here. Across all angles of attack, maximum error is approximately 21% when comparing wake survey calculations to force balance results for drag and to within 8.6% for lift. Peak error for lift occurred for the maximum scallop configuration at $\alpha = 0.6$ degrees while the peak error for drag occurred for the clean leading edge configuration at $\alpha = 0.6$ degrees. The RMS values show that the wake survey analysis of the maximum scallop configuration had the worst agreement to the balance for lift and drag. Higher RMS errors for both lift and drag occur for more severe icing configurations.

Table 2. Comparison of lift and drag results from wake survey and force balance. All results shown for tests with $\alpha = 4.8$ degrees, $Re = 1.6 \times 10^6$, and $M = 0.18$.

Icing Configuration	Lift Error (%)	Drag Error (%)	Lift RMS Error (%)	Drag RMS Error (%)
Clean Leading Edge	0.82	8.43	2.08	10.46
Maximum Scallop	7.23	16.01	6.27	15.74
Low-Fidelity Streamwise Shape with Grit	1.11	8.73	1.80	7.00
Low-Fidelity Maximum Scallop with Grit	6.82	13.05	5.81	12.64

Both lift and drag values as calculated by the wake survey are affected by several factors. The interpolation of data onto the rectangular grid introduced some amount of error. Though this is small between each point, if there is a bias in the interpolation, then this error would accumulate. Taking rectangular data would increase test time and cost significantly. Thus, this error must be balanced against test efficiency. Taking rectangular data is possible, though some error could still occur due to the likely misalignment between the desired data grid and the actual data points taken, as collecting data in a perfectly rectangular grid is essentially impossible.

A large source of error in the wake survey analysis comes as a result of the flow interaction between the wing wake and the boundary layer of the splitter plate. The splitter plate is non-metric, and thus its drag is not accounted for by the force balance. However, a boundary layer develops over the plate; this layer separates and draws low-momentum fluid upward and into the wing wake area. Thus, the momentum loss in the flow due to the splitter plate cannot be separated from the momentum loss due to drag from the wing, and the probes downstream of the wing pick up the losses generated by the plate and wing together. This effect is difficult to account for, and is in part why the wake survey tends to calculate higher drag than the force balance measures. It is possible to remove data from the wake survey analysis to account for this interaction; however, some wing wake data would be lost as well. Thus, no data were removed from this analysis with the understanding that error can be attributed to this interaction effect. An analysis was conducted to show the effect of removing wake survey data near the wing/splitter plate junction. The results for the error between the calculated lift and drag and the force balance measurements of several icing configurations at $\alpha = 4.8$

degrees, $Re = 1.6 \times 10^6$, and $M = 0.18$ are shown in Fig. 17. Equation 9 was dimensionalized using the local chord to create the lift distribution that was used to conduct this data-removal analysis. Of immediate note is that the five-hole probe array does not reach to the bottom of the wing during testing; thus, all calculations were done without 1.83% of the span nearest the root considered. All errors for lift increase at a similar rate; the same is true for drag. All errors in lift started positive, with both fidelities of the maximum scallop shape following similar trends. A positive error indicates that the wake survey calculations resulted in lift or drag higher than what the force balance measured, while a negative error indicates the opposite. The clean leading edge and low-fi streamwise with grit shape also followed similar curves. Though the drag errors for these configurations started at different initial values, they tended to change at the same rate. The low-fi streamwise with grit shape and clean leading edge configurations both had initial drag errors below zero, indicating that the wake survey calculated drag below what the force balance measured, even when no data was removed. Though reducing the amount of error from the interaction between the wing wake and the boundary layer from the splitter plate is possible, separating the flows completely is not possible. Thus, some amount of error will exist with the wake survey system due to this effect.

Though likely small, another potential source of error is the effect of turbulence on the analysis. This source of error is two-fold. First, the integrals for lift and drag components neglect the Reynolds stress term that accounts for turbulent fluctuations in the flow. Neglecting these terms may not be a valid assumption for the iced wing, especially at larger angles of attack. Secondly, turbulent velocity fluctuations in the flow contaminate pressure measurements due to the nonlinear relation between pressure and velocity as well as affect the angular response of the probe. These effects cause errors in the measured total pressure, velocity, and flow angularity. Though these effects are not considered in this analysis, they do exist. The effect of turbulence on five-hole probes can be explained physically. Standard five-hole probes place a pressure transducer relatively far from the location of the pressure measurement and long tubing between these points creates a dampening effect of the pressure measurement as it changes rapidly over time due to turbulence. This rapid oscillation cannot be measured through the long tubing. Error due to turbulence is more likely to manifest at higher angles of attack (especially stall conditions) as well as with iced configurations. These effects were explored in more detail by Diebold[19] but are not considered in this study.

B. Spanwise Force Distributions

Figures 18 and 19 show spanwise distributions of the drag components and lift, respectively, for the wing with a clean leading edge at $\alpha = 4.8$ degrees. The sectional drag coefficient distribution has been split into sectional profile drag coefficient and sectional induced drag coefficient. Distinct aerodynamic features can be seen from the oil distribution; the bright oil region near the leading edge indicates flow separation, while the dark area downstream indicates flow reattachment. Starting at a spanwise location of approximately y/b = 0.6, a secondary separation and reattachment region can be seen, as indicated by a second bright and dark region downstream of the first. Near the wing tip, a bright region is seen; this is the oil reacting to the wing tip vortex. Looking at the drag distributions, this is the region where both profile and induced drag increase sharply. This is expected, as there is a greater momentum loss near the wing tip due to the wing tip vortex. Near the wing root, there is an increase in the profile drag as well. The increased cross-section size of the wing causes an increase in skin friction as well as form drag. Ideally, these combined effects alone produced the increase in profile drag. However, the increase in profile drag is large, and most of the increase in profile drag is likely due to the interaction between the wing wake and splitter plate boundary layer.

The spanwise sectional lift coefficient distribution shows a change in the slope of the curve near the Yehudi break (at a spanwise location of about y/b = 0.27). This is because of the sharp change in chord length at this point. Overall, the local sectional lift coefficient increases until a spanwise location of about y/b = 0.6, where it slowly begins to decrease until a sharp drop near the wing tip. Figure 20 shows the contour plot of the velocity deficit in the wake of the wing. As anticipated, the deficit is greatest in the middle of the wake where physical flow blockage due to viscous effects is greatest.

These results are compared to similar results for the wing with leading edge ice shapes. Figures 21 through 23 show results for the wing at the same Reynolds number and angle of attack, but with a maximum scallop ice shape attached to the leading edge. The oil visualization shows distinct streamwise vortices that are the result of the gaps in the ice shape; these gaps are visible in Fig. 2(a). The spanwise drag curve shows some of this periodicity, most apparent from y/b = 0.35 to y/b = 0.5. The same sharp increase in drag is seen near the wing tip, however the magnitude is higher, with the peak of induced drag at approximately 0.17. Most of the increase in drag is due to an increase in the profile drag due to separated flow behind the ice

shape. The sectional lift distribution, shown in Fig. 22, follows a similar trend to the clean leading edge configuration. The peak of the sectional lift coefficient distribution occurs near the Yehudi break, where the value of sectional lift coefficient is approximately 0.48; this is lower than that of the clean leading edge, which peaked at about 0.51. Figure 23 shows the contour plot of the velocity deficit for the maximum scallop leading edge configuration. Concentrations of lowered velocity occur periodically starting approximately at spanwise location y/b = 0.55 and continue to the wing tip. These regions may be the result of the distinct streamwise vortices that are seen in the oil flow imagery. A one-to-one correlation between the streamwise vortices and the velocity deficit concentrations is not seen, however. This indicates the possibility of vortex interactions. This effect is coupled with the diffusion of the vortices, making them harder to detect downstream of the wing. The exact rotational orientation of these vortices cannot be discerned from the collected data. One possible explanation for the observed spacing of the velocity deficit concentrations is that the vortices coalesce downstream of the trailing edge and create the periodic pattern seen. To make these areas more distinct, the wake survey plane would have to be moved closer to the trailing edge of the wing, and the resolution of the wake survey increased.

Figures 24 to 27 show the spanwise distributions for drag components and lift, as well as the velocity deficit contour plot for the low-fi maximum scallop ice shape with grit. The data show a similar increasing trend, but with large oscillatory behavior. The largest oscillations occur at y/b = 0.65 and approximately y/b = 0.75. The most prominent feature in the high-fidelity maximum scallop shape are the small streamwise vortices that develop across the span of the wing. These vortices potentially manifest as small oscillations in the spanwise distribution data as well as periodic regions of relatively high velocity deficits. The spanwise sectional drag distributions for the low-fi maximum scallop with grit configuration, Fig. 24, do not show the same small periodic oscillation that the high-fidelity case does, but do show large oscillations due to large leading edge vortices; these vortices do not form due to gaps in the shape, as there are no gaps in the low-fi shape (see Fig. 2(b)). Looking at the oil flow, there is a large region of separation near the leading edge from y/b = 0.5 to the wing tip(indicated by an accumulation of oil). This separation, due to the ice shape, causes the formation of large vortices seen in the oil flow in the same spanwise region. The vortices in the high-fidelity maximum scallop configuration are a result of the gaps in the shape. Thus, the oscillations seen in the low-fi maximum scallop shape are not comparable to the smaller, periodic streamwise vortices seen in the high-fidelity case. A comparison between the total sectional drag coefficient distributions for the two fidelities is shown in Fig. 25. The sectional lift coefficient distribution, given in Fig. 26, compares the low-fi maximum scallop with grit configuration to the high-fidelity maximum scallop configuration. It also shows large oscillations in the same regions as the sectional drag coefficient distributions. The velocity deficit contour for the low-fi maximum scallop with grit configuration in Fig. 27 shows that there are large concentrations of velocity deficit that align with the large oscillations seen in the spanwise distributions. The low-fi maximum scallop shape does not maintain a flowfield similar to the high-fidelity maximum scallop at all.

The low-fi streamwise with grit shape is expected to have different results, as the ice shape is more streamlined than the highly 3D features of the maximum scallop shapes; a computerized view of the low-fi streamwise shape is shown in Fig. 12. The results for the low-fi streamwise with grit shape configuration are given in Fig. 28 to Fig. 30. No oil flow was conducted for this ice configuration at $\alpha = 4.8$ degrees. Figures 28 and 29 show relatively smooth curves from wing root to tip, comparable to the clean leading edge configuration. This is also seen in the velocity deficit plot, Fig. 30. The wake maintains a uniform spanwise pattern from the upper surface of the wing to the lower surface with minimal disruption until the wing tip.

It is seen from the spanwise drag coefficient distributions for the four configurations considered that profile drag tends to be higher than induced drag for most of the span, except near the wing tip. Most error in the total drag likely comes from the profile drag, which in turn is affected heavily by the low momentum fluid from the splitter plate boundary layer being captured in the wake survey. Thus, errors in the pressure and velocity measurements, which profile drag depends as per Eq. 2, manifest as error in the total drag. There is likely some error in the vorticity calculation as well, causing error in induced drag. This error would also manifest as error in the stream function. However, induced drag is a much smaller component of the total drag for the considered configurations, and is likely not a major source of error in the results. The flow interaction between the wing wake and the splitter plate boundary layer, as well as error in the vorticity calculations due to velocity measurement errors in the flow, are the likely cause of errors in the lift calculated using the wake integrals.

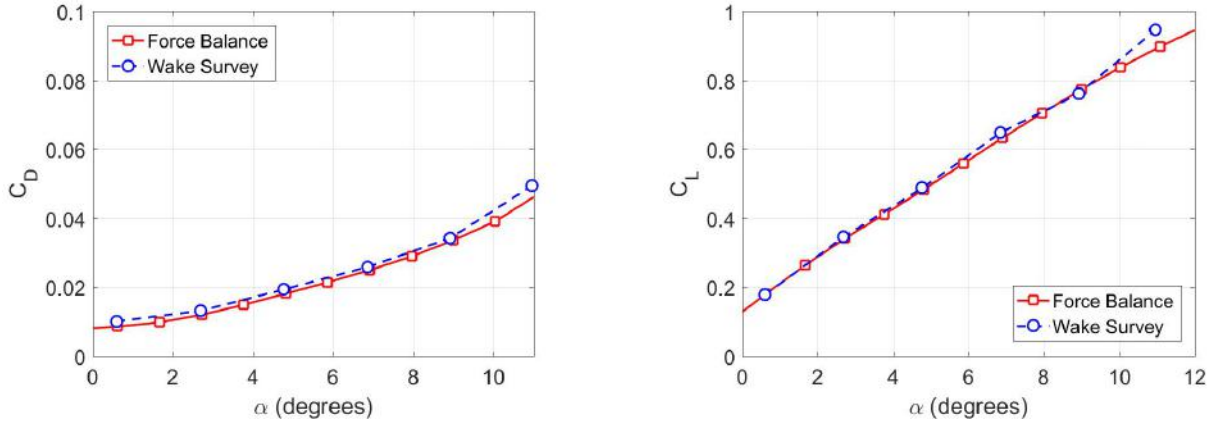

(a) Drag coefficient versus α.

(b) Lift coefficient versus α.

Figure 13. Comparison of wake survey and force balance data for clean leading edge configuration.

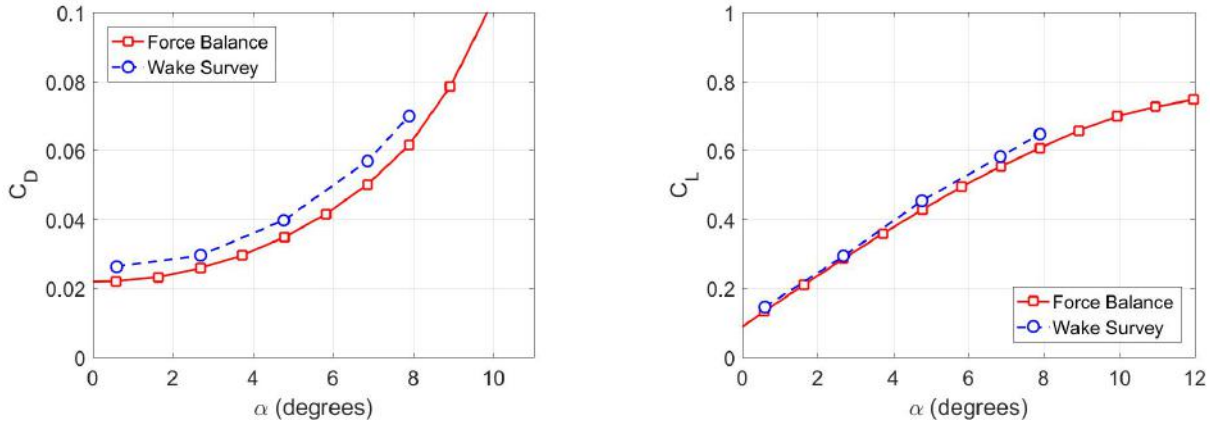

(a) Drag coefficient versus α.

(b) Lift coefficient versus α.

Figure 14. Comparison of wake survey and force balance data for maximum scallop configuration.

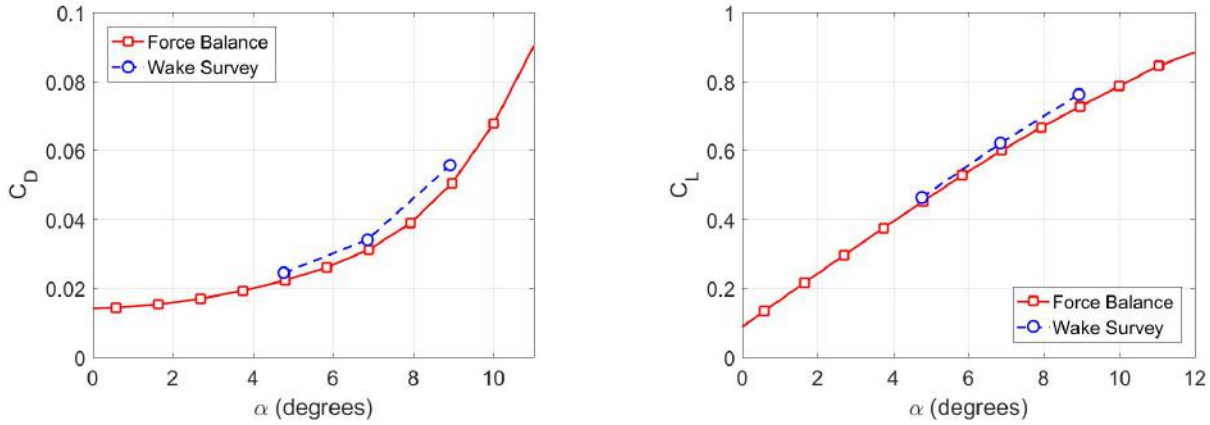

(a) Drag coefficient versus α.

(b) Lift coefficient versus α.

Figure 15. Comparison of wake survey and force balance data for the low-fidelity streamwise with grit configuration.

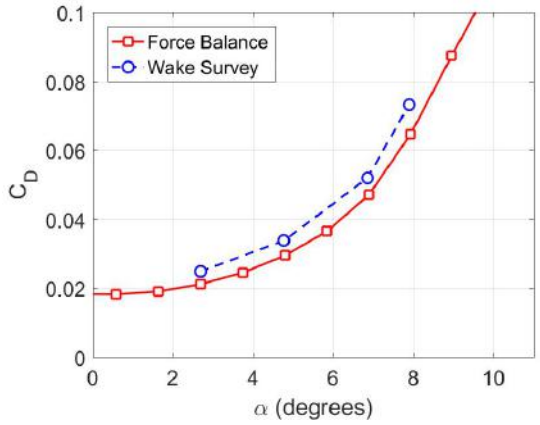

(a) Drag coefficient versus α.

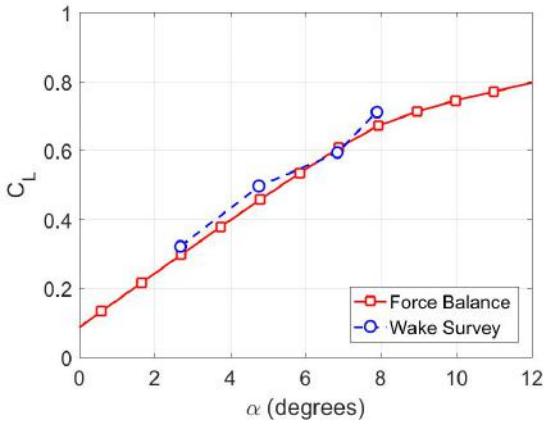

(b) Lift coefficient versus α.

Figure 16. Comparison of wake survey and force balance data for the low fidelity maximum scallop with grit configuration.

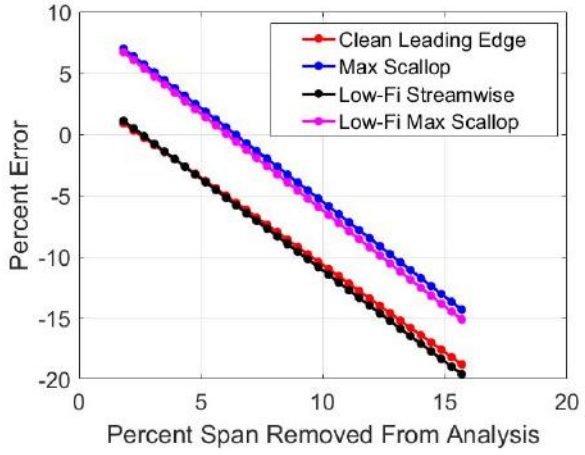

(a) Lift error versus percent of wing span removed from analysis.

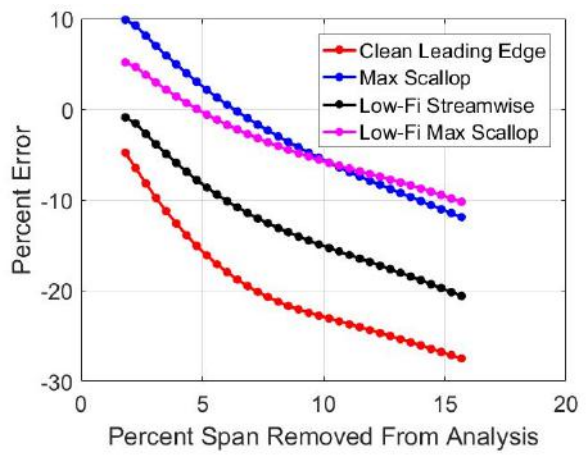

(b) Drag error versus percent of wing span removed from analysis.

Figure 17. Percent error between the wake survey calculations and force balance measurements as a function of amount of wake data removed from wing/splitter plate junction, given as percentage span of the wing. All cases were at $\alpha = 4.8$ degrees, $Re = 1.6 \times 10^6$, and $M = 0.18$.

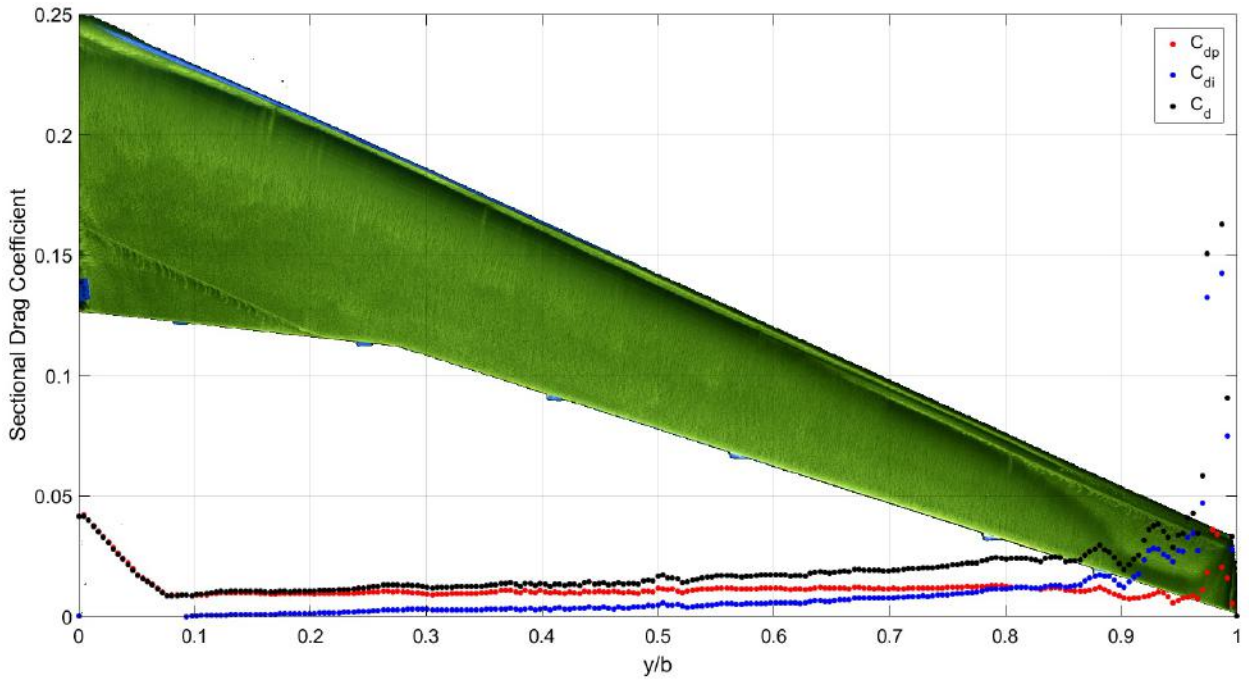

Figure 18. Spanwise distribution of sectional induced, profile, and total drag coefficients for clean leading edge configuration at $\alpha = 4.8$ degrees, $Re = 1.6 \times 10^6$, and $M = 0.18$, laid over oil flow imagery for the configuration.

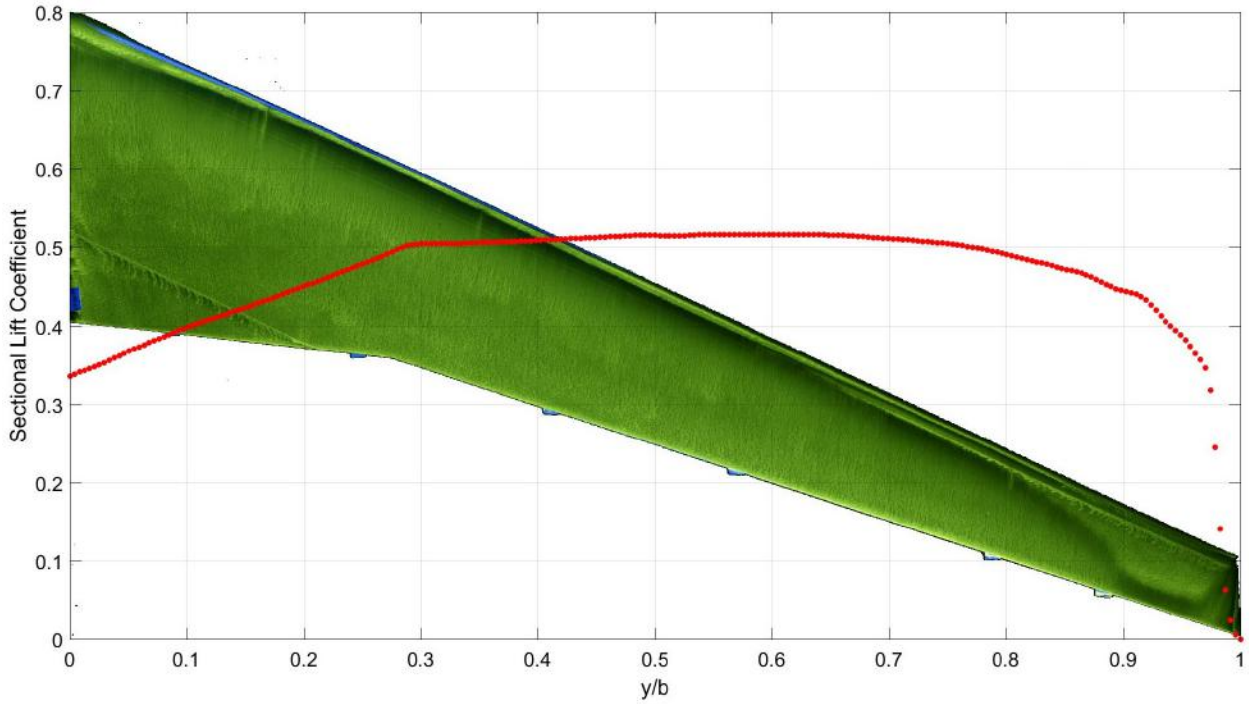

Figure 19. Spanwise distribution of sectional lift coefficient for clean leading edge configuration at $\alpha = 4.8$ degrees, $Re = 1.6 \times 10^6$, and $M = 0.18$, laid over oil flow imagery for the configuration.

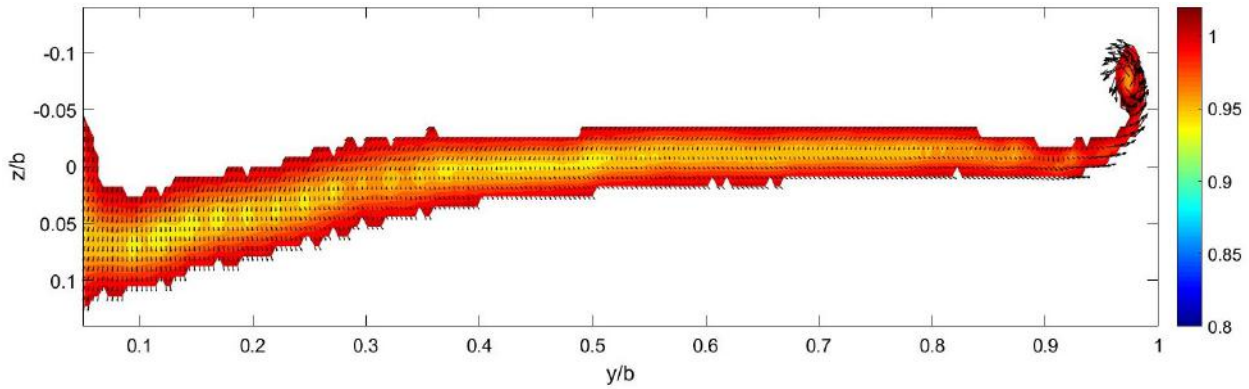

Figure 20. Contour plot of velocity deficit for clean leading edge configuration at $\alpha = 4.8$ degrees, $Re = 1.6 \times 10^6$, and $M = 0.18$.

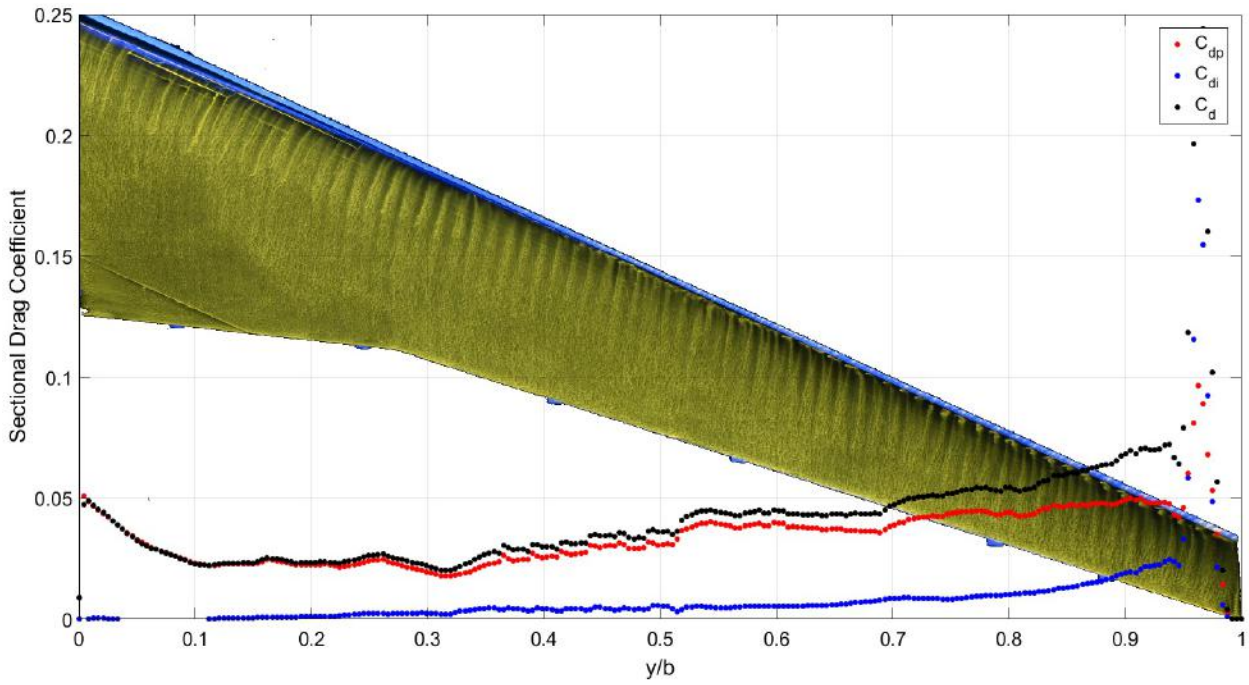

Figure 21. Spanwise distribution of sectional induced, profile, and total drag coefficients for the maximum scallop configuration at $\alpha = 4.8$, $Re = 1.6 \times 10^6$, and $M = 0.18$, degrees laid over oil flow imagery for the configuration.

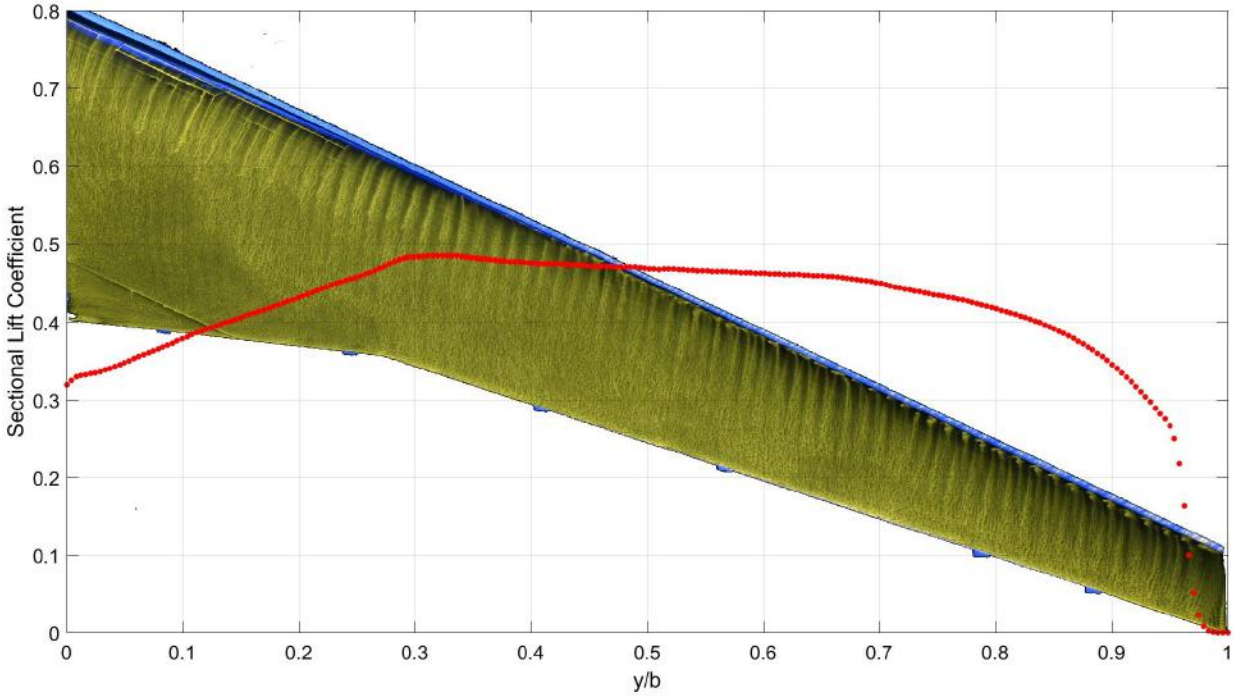

Figure 22. Spanwise distribution of sectional lift coefficient for the maximum scallop configuration at $\alpha = 4.8$, $Re = 1.6 \times 10^6$, and $M = 0.18$, degrees laid over oil flow imagery for the configuration.

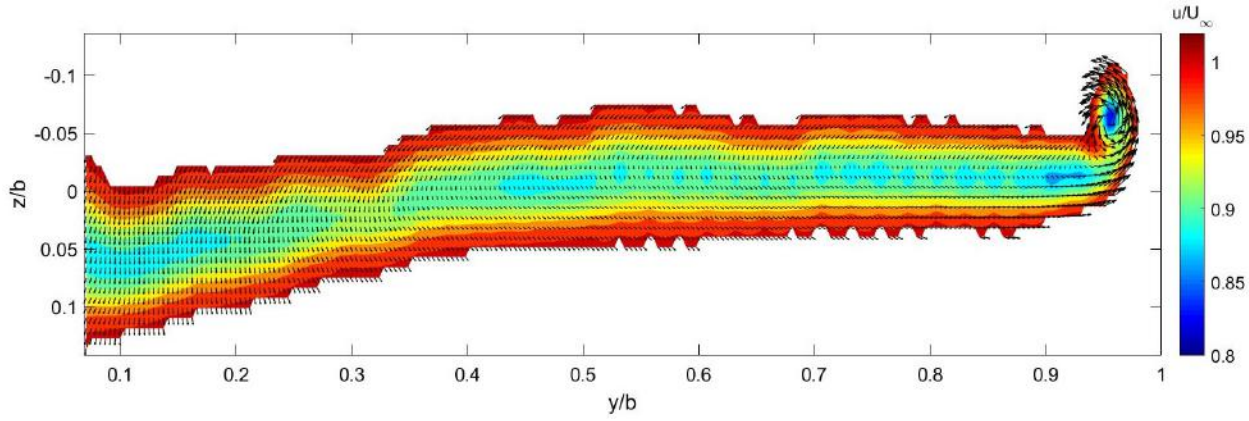

Figure 23. Contour plot of velocity deficit for the maximum scallop configuration at $\alpha = 4.8$ degrees, $Re = 1.6 \times 10^6$, and $M = 0.18$.

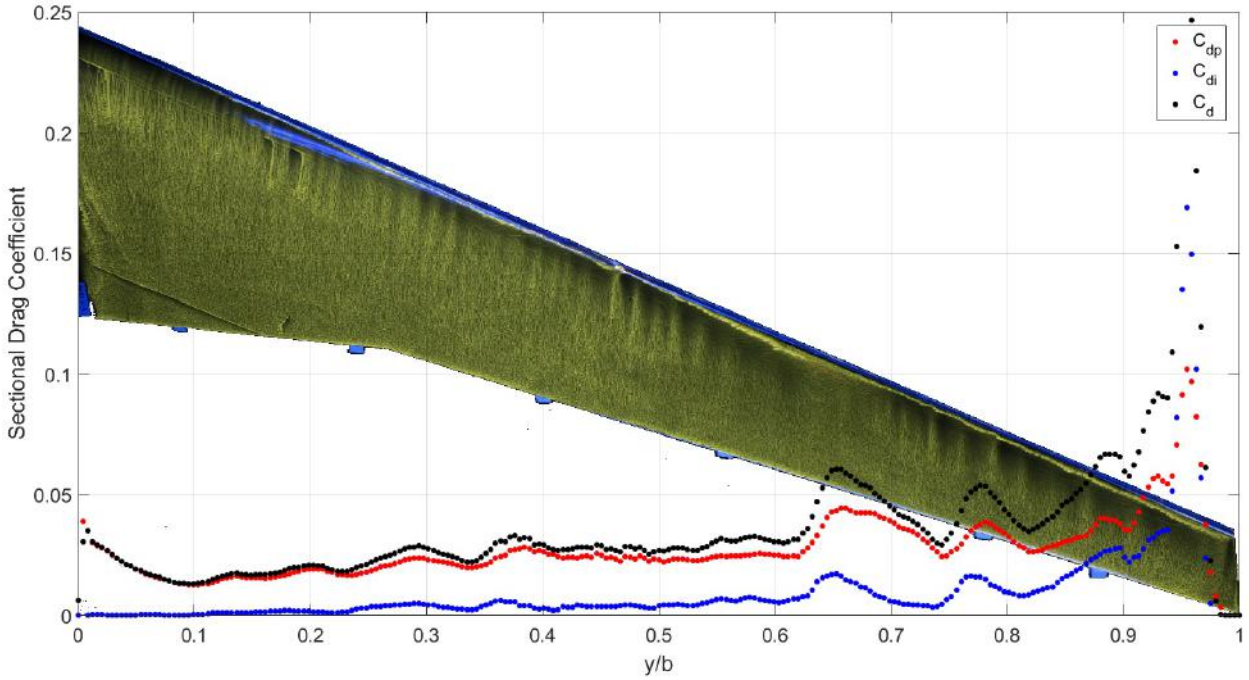

Figure 24. Spanwise distribution of sectional induced, profile, and total drag coefficients for the low-fi maximum scallop with grit configuration at $\alpha = 4.8$ degrees, $Re = 1.6 \times 10^6$, and $M = 0.18$.

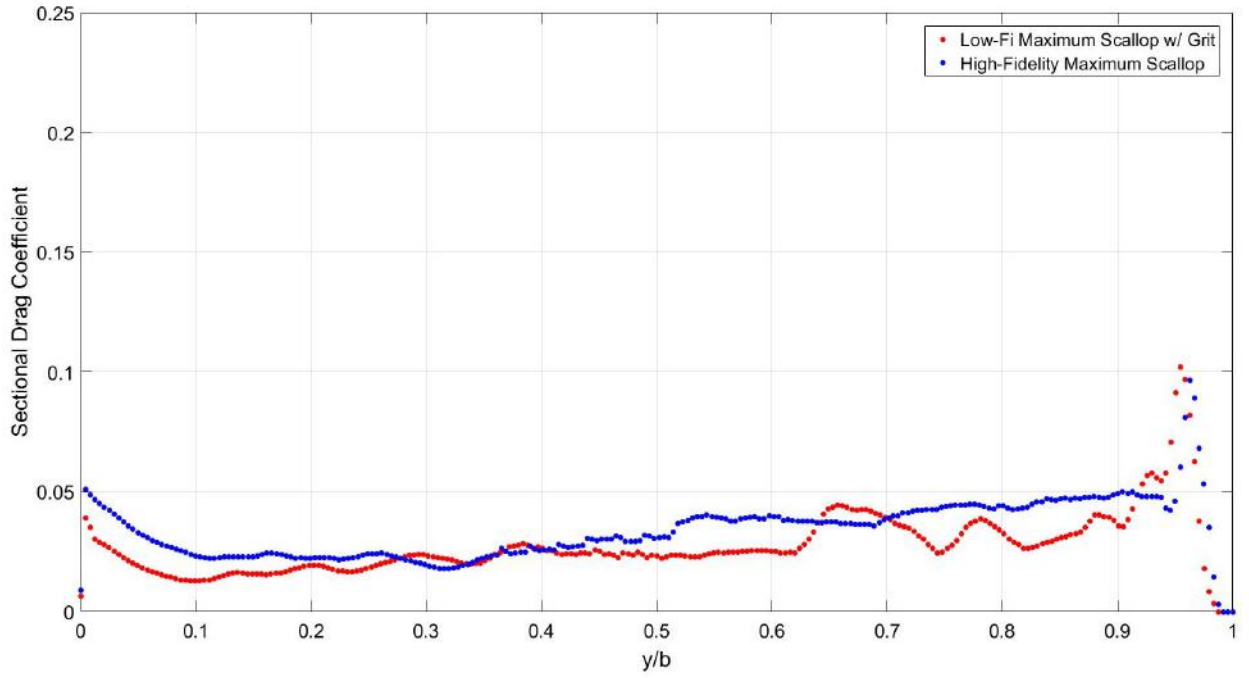

Figure 25. Spanwise distributions of total sectional drag coefficient for the low-fi maximum scallop with grit and the high-fidelity maximum scallop configurations at $\alpha = 4.8$ degrees, $Re = 1.6 \times 10^6$, and $M = 0.18$.

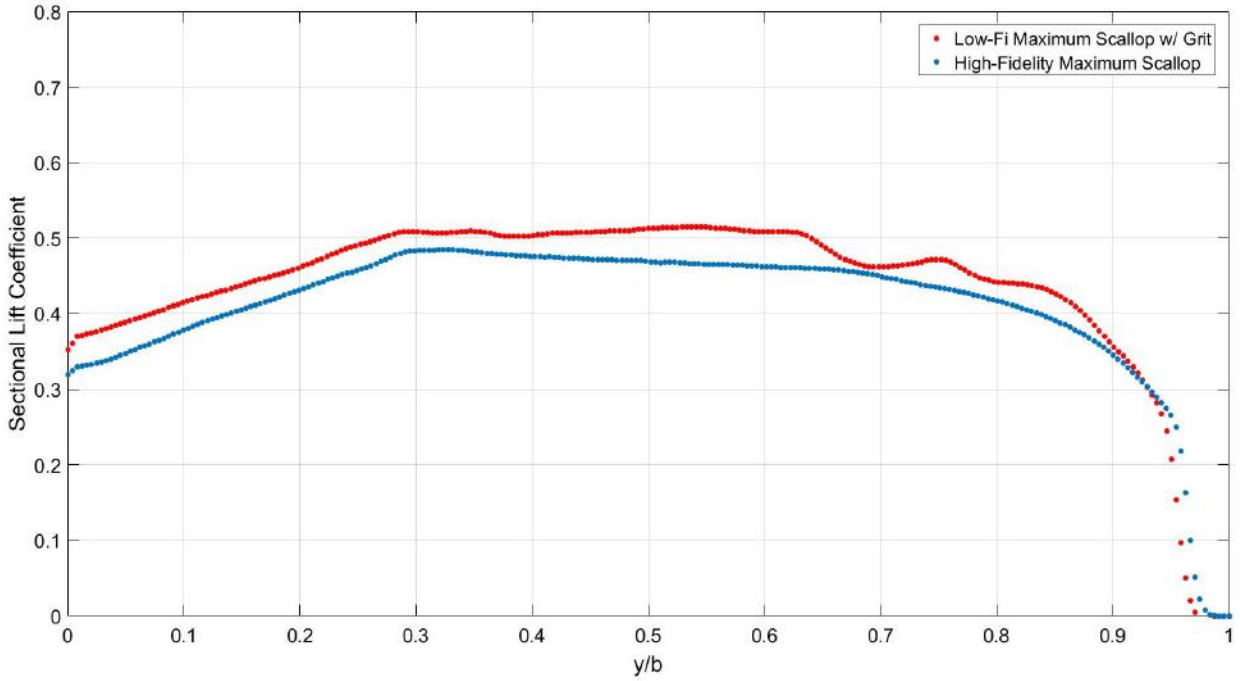

Figure 26. Spanwise distributions of sectional lift coefficient for the low-fi maximum scallop with grit and the high-fidelity maximum scallop configurations at $\alpha = 4.8$ degrees, $Re = 1.6 \times 10^6$, and $M = 0.18$. Note that no oil flow is shown as the flowfield differs between each fidelity.

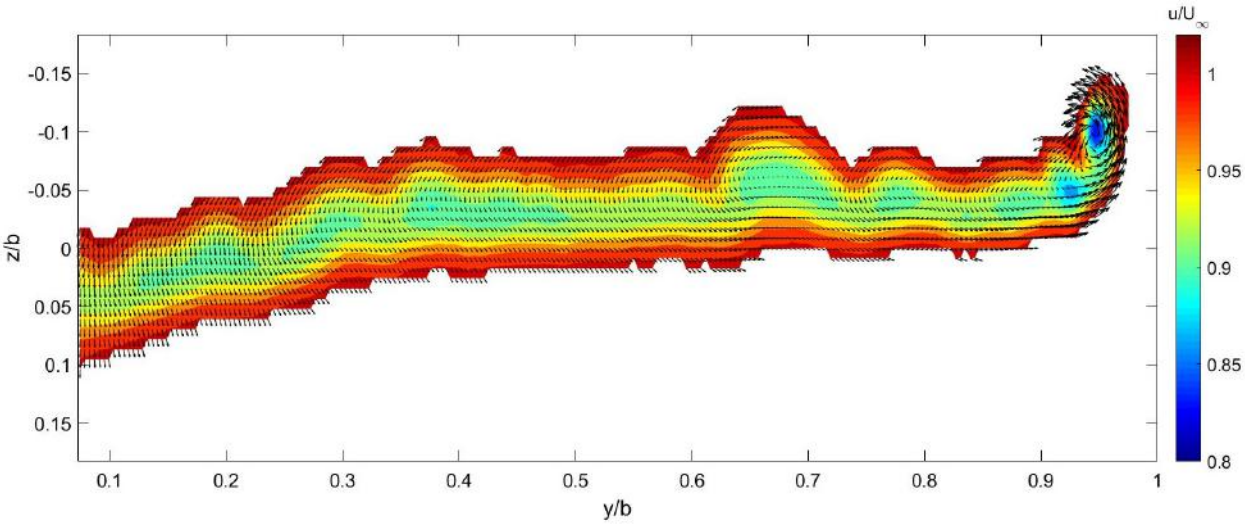

Figure 27. Contour plot of velocity deficit for the low-fi maximum scallop with grit configuration at $\alpha = 4.8$ degrees, $Re = 1.6 \times 10^6$, and $M = 0.18$.

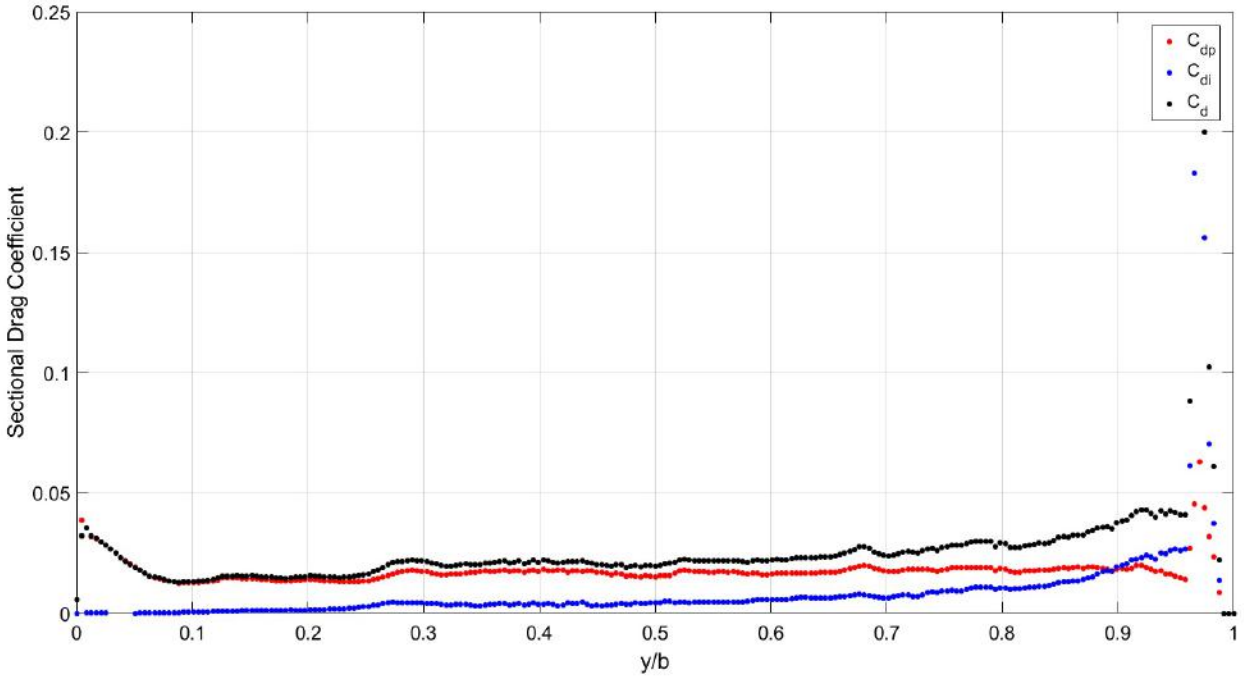

Figure 28. Spanwise distribution of sectional induced, profile, and total drag coefficients for the low-fi streamwise with grit configuration at α = 4.8 degrees, $Re = 1.6 \times 10^6$, and M = 0.18.

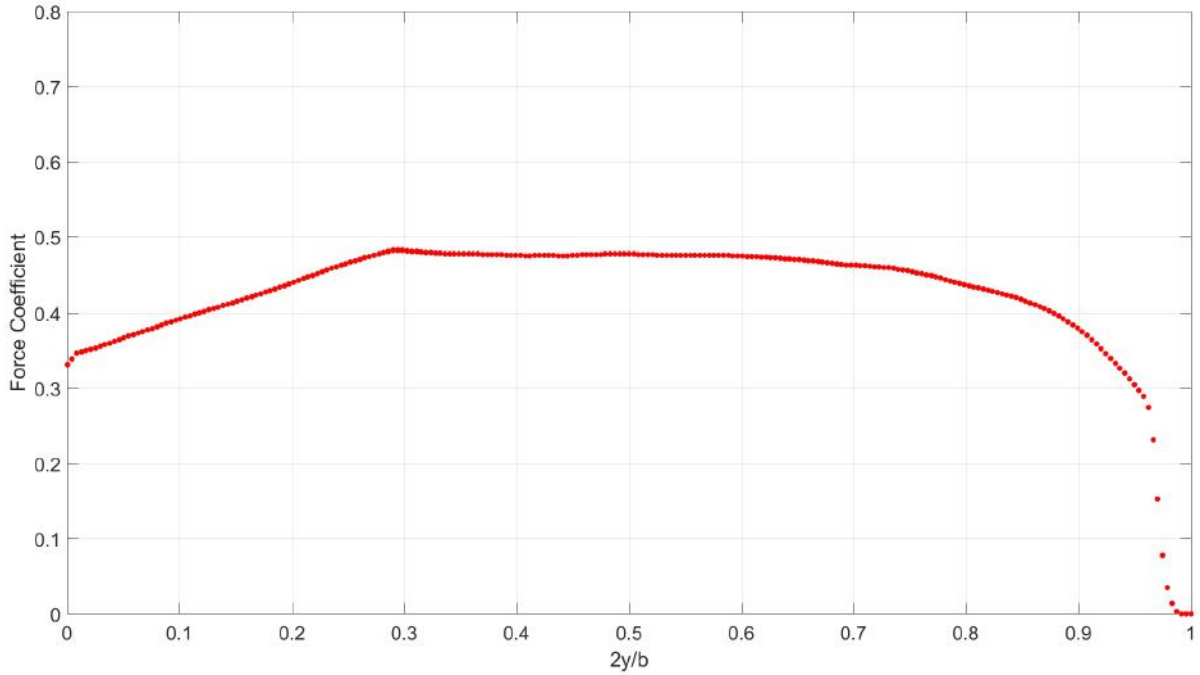

Figure 29. Spanwise distribution of sectional lift coefficient for the low-fi streamwise with grit configuration at α = 4.8 degrees, $Re = 1.6 \times 10^6$, and M = 0.18.

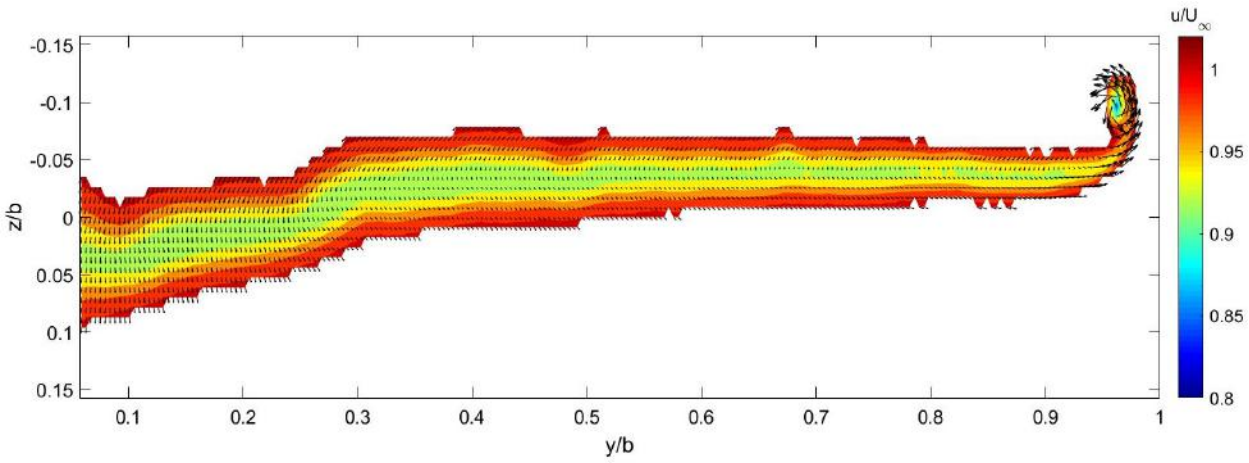

Figure 30. Contour plot of velocity deficit for the low-fi streamwise with grit configuration at $\alpha = 4.8$ degrees, $Re = 1.6 \times 10^6$, and $M = 0.18$.

VII. Conclusions and Future Research

This paper presents a method for utilizing five-hole probes to survey the wake of a swept wing model with ice accretions. This method can be used to enhance understanding of the flowfield on iced aircraft and the ramifications on aerodynamic performance.

Some future work would include increasing the accuracy of the probe locations measurements. As seen previously, accurate placement of the probes is not as important as accurate measurement of their actual locations due to the fine spatial resolution and precision required to resolve some of the flowfield features. The laser tracking system directly measured the position of the origin of the traverse frame, F_T (Figure 5(b)). However, the laser was shone through the window of the test section, which introduces minor errors due to the refraction of the glass. Wind-off data was taken with the window installed and removed. This data can be used in future work to generate a correction for the window refraction. On a similar note, during wind-on testing, the wake survey array was subject to non-trival aerodynamic loads, possibly bending and deflecting the probe array. The position of the array was measured using the laser tracking system but the relative rotation of the array was not. Future work would include correcting for the possible rotation of the array.

The aerodynamic performance of an iced wing was extracted from wake survey data reasonably well. Total lift had errors ranging from 0.8% to 8.6% when comparing the wake survey calculations to force balance measurements. Total drag had errors ranging from 3.2% to 21%. RMS errors show that for all angles of attack tested, the maximum scallop configuration had the worst agreement between wake survey calculations and force balance measurements for both lift and drag (6.27% and 15.74%, respectively). Errors in the wake survey system were caused chiefly by splitter plate effects limiting the amount of unspoiled wake data that could be integrated. Future studies should include a method to minimize the amount of contaminated wake data. Data interpolation was also a source of error; this could be minimized by taking data in a rectangular grid during the experiment or by decreasing the spacing between data points. However, this increases both test time and cost, and because the error is assumed small, is not recommended. Some error was attributed to turbulence, due to neglecting the Reynolds stress term and turbulent effects on the five-hole probes. Further studies should investigate the use of fast-response five-hole probes to characterize and minimize the effect of turbulence on probe measurements for iced swept-wing configurations.

Lift and drag coefficient calculations from the wake survey agreed well with the force balance with changing angle of attack. The spanwise distributions for sectional profile and induced drag coefficients seemed to show a reaction to apparent streamwise vortices generated as a result of the maximum scallop ice shape. However, individual vortices did not seem to appear in the spanwise calculations, possibly due to vortex interaction causing multiple streamwise vortices to coalesce. Future studies should investigate the effect of moving the wake survey plane closer to the trailing edge of the wing to see if these vortices could be captured by the wake survey method, and if the velocity deficit concentrations become more pronounced. The streamwise vortices are found in both fidelities of the maximum scallop shape, but are formed through different mechanisms, and thus the low-fi maximum scallop with grit ice shape cannot be used to produce a good aerodynamic approximation of the high-fidelity maximum scallop shape. The spanwise sectional drag coefficients also increased sharply near the wing tip in all cases, likely reacting to the wing tip vortex. Further studies should increase the resolution of the wake survey in this region. Future work will analyze results from all ice shapes and angles of attack tested.

Acknowledgments

The authors would like to thank other members of the research team including Andy Broeren, Sam Lee, Mark Potapczuk from NASA for their contributions to the test preparation and execution.

Many members at the UW Aircraft Icing and Aerodynamics Research Group such as Stephanie Camello, Gustavo Fujiwara, Kevin Ho, Julian Woo, Ahrif McKee, Yik Sang Yu, Lenny Lin, Rami Slim, Jessica Hsu, Andrew Kang, Kevin Choi, Bobby Huynh, Reuben Straus, Abijit Arun, Trevor Hedges, Shringar Shamkuwar, Carter Gilmour, Mircea Cozmei, Nicholas Price, and Tyler Omoto.

John Laffen, Kevin Kelly, Aaron Kuen, and Ryan Benyshek at the Walter H. Beech Memorial Wind Tunnel at Wichita State University were immensely helpful with test preparation, execution, and data acquisition.

The authors would also like to thank James Riley and Timothy Smith from the FAA for their contributions to the project. This work was funded by the FAA grant 15-G-009.

References

[1]Khodadoust, A. and Bragg, M. B., "Aerodynamics of a Finite Wing with Simulated Ice," *Journal of Aircraft*, Vol. 32, No. 1, 1995, pp. 137–144.

[2]Bragg, M. B., Kerho, M. F., and Khodadoust, A., "LDV Flowfield Measurements on a Straight and Swept Wing with a Simulated Ice Accretion," *AIAA Paper 93-0300*, 1993.

[3]Bragg, M. B., Broeren, A. P., and Blumenthal, L. A., "Iced-Airfoil Aerodynamics," *Progress in Aerospace Sciences*, Vol. 41, No. 5, 2005, pp. 323–362.

[4]Diebold, J. M., Broeren, A. P., and Bragg, M. B., "Aerodynamic Classification of Swept-Wing Ice Accretion," *Proceedings of the 5th AIAA Atmospheric and Space Environments Conference*, San Diebo, CA, June 2013.

[5]Diebold, J. M., Monastero, M. C., and Bragg, M. B., "Aerodynamics of a Swept Wing with Ice Accretion at Low Reynolds Number," *Proceedings of the 30th AIAA Applied Aerodynamics Conference*, New Orleans, LA, June 2012.

[6]Fujiwara, G. E., Woodard, B. S., Wiberg, B., Mortonson, A. J., and Bragg, M. B., "A Hybrid Airfoil Design Method for Icing Wind Tunnel Tests," *Proceedings of the 5th AIAA Atmospheric and Space Environments Conference*, 2013.

[7]Fujiwara, G. E., Wiberg, B. D., Woodard, B. S., and Bragg, M. B., "3D Swept Hybrid Wing Design Method for Icing Wind Tunnel Tests," *Proceedings of the 6th AIAA Atmospheric and Space Environments Conference*, 2014.

[8]Broeren, A. P., Potapczuk, M. G., Lee, S., Malone, A. M., Paul Jr., B. P., and Woodard, B. S., "Ice-Accretion Test Results for Three Large-Scale Swept-Wing Models in the NASA Icing Research Tunnel," *Proceedings of the 8th AIAA Atmospheric and Space Environments Conference*, June 2016.

[9]Camello, S. C., Lee, S., Lum, C. W., and Bragg, M. B., "Generation of Fullspan Leading-Edge 3D Ice Shapes for Swept-Wing Aerodynamic Testing," *Proceedings of the 8th AIAA Atmospheric and Space Environments Conference*, June 2016.

[10]Radenac, E., "Validation of a 3D Ice Accretion Tool on Swept Wings of the SUNSET2 Program," *Proceedings of the 8th AIAA Atmospheric and Space Environments Conference*, June 2016.

[11]Wiberg, B. D., Fujiwara, G. E. C., Woodard, B. S., and Bragg, M. B., "Large-Scale Swept-Wing Icing Simulations in the NASA Glenn Icing Research Tunnel Using LEWICE3D," *Proceedings of the 6th AIAA Atmospheric and Space Environments Conference*, 2014.

[12]Fujiwara, G. E. C., Bragg, M. B., Camello, S., and Lum, C. W., "Computational and Experimental Ice Accretions of Large Swept Wings in the Icing Research Tunnel," *Proceedings of the 8th AIAA Atmospheric and Space Environments Conference*, June 2016.

[13]Butler, C., Qin, C., and Loth, E., "Improved Delayed Detached-Eddy Simulation on a Swept Hybrid Model in IRT," *Proceedings of the 8th AIAA Atmospheric and Space Environments Conference*, June 2016.

[14]Fujiwara, G. E. C. and Bragg, M. B., "3D Computational Icing Method for Aircraft Conceptual Design," *Submitted to the 9th Atmospheric and Space Environments Conference*, Denver, CO, June 2017.

[15]Broeren, A. P., Woodard, B. S., Diebold, J. M., and Moens, F., "Low-Reynolds Number Aerodynamics of an 8.9Wing for Assessment of Icing Effects," *Submitted to the 9th Atmospheric and Space Environments Conference*, Denver, CO, June 2017.

[16]Camello, S. C., Bragg, M. B., Broeren, A. P., Lum, C. W., Woodard, B. S., and Lee, S., "Effect of Ice Shape Fidelity on Swept-Wing Aerodynamic Performance," *Submitted to the 9th Atmospheric and Space Environments Conference*, Denver, CO, June 2017.

[17]Diebold, J. M. and Bragg, M. B., "Study of a Swept Wing with Leading-Edge Ice Using a Wake Survey Technique," *Proceedings of the 51st AIAA Aerospace Sciences Meeting*, Grapevine, TX, January 2013.

[18]Diebold, J. M., *Aerodynamics of a Swept Wing with Leading-Edge Ice at Low Reynolds Number*, Master's thesis, University of Illinois at Urbana-Champaign, Urbana, Illinois, 2012.

[19]Diebold, J. M., *The Effects of Turbulence on the Measurements of Five-Hole Probes*, Ph.D. thesis, University of Illinois at Urbana-Champaign, Urbana, IL, 2017.

[20]Lynch, F. T. and Khodadoust, A., "Effects of Ice Accretion on Aircraft Aerodynamics," *Progress in Aerospace Sciences*, Vol. 37, No. 8, 2001, pp. 669–767.

[21]Papadakis, M., Yeong, H.-W., and Wong, S.-C., "Aerodynamic Performance of a Wwept Wing with Ice Accretions," *Proceedings of the 41st AIAA Aerospace Sciences Meeting and Exhibit*, Reno, NV, 2003.

[22]Papadakis, M., Yeong, H.-W., and Wong, S.-C., "Aerodynamic Performance of a Wwept Wing with Simulated Ice Shapes," *Proceedings of the 42nd AIAA Aerospace Sciences Meeting and Exhibit*, 2004.

[23]Vassberg, J. C., DeHaan, M. A., Rivers, S. M., and Wahls, R. A., "Development of a Common Research Model for Applied CFD Validation Studies," *Proceedings of the 26th AIAA Applied Aerodynamics Conference*, Honolulu, HI, August 2008.

[24]Diebold, J. M., Woodard, B. S., Monastero, M. C., and Bragg, M. B., "Experimental Study of Splitter Plates for Use with Semispan Wing Models," *Proceedings of the 53rd AIAA Aerospace Sciences Meeting*, Kissimmee, FL, January 2015.

[25]Woodard, B. S., Broeren, A. P., Diebold, J. M., and Bragg, M. B., "Preliminary Assessment of Low-Reynolds Number Aerodynamics for a Swept Wing with Artificial Ice Roughness," Tech. rep., Federal Aviation Administration, 2015.

[26]Johnson, B. L., "Facility Description of the Walter H. Beech Memorial 7 x 10 foot Low-Speed Wind Tunnel," Tech. rep., Wichita State University, Wichita, KS, 1993.

[27]Johnson, B. L., Leigh, J., and Moore, K., "Three-Dimensional Force Data Acquisition and Boundary Corrections for the Walter H. Beech Memorial 7 x 10 Foot Low Speed Wind Tunnel," Tech. rep., Wichita State University, Wichita, KS, 1993.

[28]Winkler, J. F., *Local Flowfield about Large Distributed Roughness Elements in a Laminar Boundary Layer*, Ph.D. thesis, University of Illinois at Urbana-Champaign, Urbana, IL, 1996.

[29]"Leica T-Scan 5," `http://metrology.leica-geosystems.com/en/Leica-T-Scan-5_105434.htm`, 2016, Online, accessed October 10, 2016.

[30] "Leica Absolute Tracker AT901," http://www.leica-geosystems.no/no/Leica-Absolute-Tracker-AT901_69047.htm, 2016, Online, accessed October 10, 2016.

[31] Treaster, A. L. and Yocum, A. M., "The Calibration and Application of Five-Hole Probes," Tech. rep., Pennsylvania State University, 1978.

[32] Paul, A. R., Upadhyay, R. R., and Jain, A., "A Novel Calibration Algorithm for Five-Hole Pressure Probe," *International Journal of Engineering, Science and Technology*, Vol. 3, No. 2, 2011, pp. 89–95.

[33] Betz, A., "A Method for the Direct Determination of Wing-Section Drag," Tech. rep., 1925.

[34] Maskell, E., "Progress Towards a Method for the Measurement of the Components of the Drag of a Wing of Finite Span," Tech. rep., 1972.